TEMPERATURE-DEPENDENT IMPACT PROPERTIES OF 3D PRINTED 15-5 STAINLESS STEEL

A Thesis

Submitted to the Faculty

of

Purdue University

by

Sugrim Sagar

In Partial Fulfillment of the

Requirements for the Degree

of

Master of Science in Mechanical Engineering

May 2018

Purdue University

Indianapolis, Indiana

THE PURDUE UNIVERSITY GRADUATE SCHOOL
STATEMENT OF COMMITTEE APPROVAL

Dr. Jing Zhang, Chair

Department of Mechanical and Energy Engineering

Dr. Andres Tovar

Department of Mechanical and Energy Engineering

Dr. Hazim El-Mounayri

Department of Mechanical and Energy Engineering

Approved by:

Dr. Jie Chen

Head of the Graduate Program

Dedicated to my beloved wife, family and friends.

ACKNOWLEDGMENTS

I would like to express my sincerest gratitude to my thesis advisor, Dr. Jing Zhang for his continuous support during my academic tenure. Dr. Zhang has been instrumental in my career transition from a practicing engineer to that of a researcher. This was made possible through his support in accessing scholarships and grants, such as the National Science Foundation (NSF) travel grant, for presentations at universities and international conferences. In addition, Dr. Zhang has been a strong advocate for the publishing of manuscripts for several conferences and internationally recognized science journals.

I would like to thank Dr. Andres Tovar and Dr. Hazim El-Mounayri for their support throughout my tenure as a graduate student and serving as part of my thesis committee.

It is with great pleasure that I would also like to highlight the contribution of PhD student Yi Zhang and Prof. David R. Johnson whom were key in executing the experimental Charpy impact test at the Mechanical Engineering Laboratory at Purdue University, West Lafayette.

I would like to acknowledge the contribution of Prof. Yeon-Gil Jung of Changwon National University, Republic of Korea for providing the Optical Micrographic (OM) and Scanning Electron Microscopy (SEM) images as well as the Energy-Dispersive X-Ray Spectroscopy (EDX) analysis.

Finally, I am ever grateful for the contribution and support from my wife, family and friends.

TABLE OF CONTENTS

Page

Page

LIST OF TABLES

LIST OF FIGURES

Figure Page

ABSTRACT

Sagar, Sugrim M.S.M.E., Purdue University, May 2018. Temperature-Dependent Impact Properties of 3D printed 15-5 Stainless Steel. Major Professor: Jing Zhang.

Since the conception of three dimensional (3D) printing circa 40 years ago, there has been the proliferation of several additive manufacturing (AM) technologies that enable its use in everyday applications such as aerospace, medicine, military, oil and gas and infrastructure. In order to improve its applicability and growth, 3D printed materials are subjected to the same or even higher levels of scrutiny on its mechanical behavior as the conventionally manufactured counterpart.

One of the most important mechanical properties is toughness or the ability of a material to undergo large strain prior to fracture when loaded. The toughness of a material can be correlated to its impact energy or the increase in internal energy due to impact.

In this study, the impact properties, including the toughness of 3D printed 15-5 stainless steel were investigated at low temperature (77 K), room temperature (298 K) and high temperature (723 K) using experimental and numerical modeling of the Charpy impact test. In addition, ballistic impact simulations were performed to determine the applicability of 3D printed 15-5 stainless steel in the defense industry.

The 15-5 stainless steel specimens were printed (horizontal-build) using the direct metal laser sintering (DMLS) technique, cooled or heated to the specified temperature, then tested in accordance with the ASTM E23-2016b [1] standard. The Johnson-Cook (J-C) phenomenological material model and fracture parameters were used in the numerical modeling. The cross-sectional microstructures of surfaces and impact energies of the Charpy impact test were examined. For the ballistic impact simulations, a 3D printed 15-5 stainless steel typical plate was investigated at the

same temperatures as the Charpy impact test. A typical missile using the J-C properties at room temperature (298 K) was assigned an initial velocity of 300 ms^{-1} for each plate temperature.

The fracture surface investigation (microsurface analysis as well as visual inspection) and impact energy values of the Charpy impact test show that the 3D printed 15-5 stainless steel exhibited brittle behavior at low and room temperatures, but transitioned into a more ductile behavior at high temperature. At 77 K, 298 K and 723 K, the experimental Charpy impact test results were 0.00 J/cm^2, 6.78±4.07 J/cm^2 and 50.84±3.39 J/cm^2 respectively whereas the simulated impact energy were 1.05 J/cm^2, 10.46 J/cm^2 and 47.07 J/cm^2 respectively. Hence, the impact energy for the experimental and numerical simulations were in good agreement; especially at higher temperatures.

Consistent with the results from the Charpy impact test, the ballistic impact simulations show an increase in the impact energy, effective plastic strain and deflection of the plate with an increase in temperature indicating brittle-to-ductile behavior. The high exit velocity at low and room temperature may not make the plate attractive in defense in its current configuration; however, at high temperature, the exit velocity reduction was significant.

1. INTRODUCTION

1.1 Background

1.1.1 Three dimensional (3D) printing

Three dimensional (3D) printing is a form of additive manufacturing that produces a 3D object from a 3D model by the controlled deposition of material in successive layers. This relatively new and rapidly emerging technology is set to revolutionize manufacturing in the near future.

Although additive manufacturing existed before the 1980's, the first recognized published work of Japanese inventor Hideo Kodama detailed the creation of an object from a 3D model [2] in 1981 and printing of plastic parts by photo-polymerization from ultraviolet (UV) exposure [3] in 1983. The first patented stereolithography (STL) 3D printer was invented by Charles "Chuck" Hull (founder of 3D Systems) in 1986 [4].

Since then, several technological processes emerged in 3D printing, such as; powder bed fusion (PBF) , electron beam modeling (EBM), fusion deposition modeling (FDM) and direct energy deposition (DED). Increase in demand for 3D printing for rapid prototyping and functional parts requires augmented research into the mechanical performance of its manufactured products. The expectation of the scientist and the entrepreneur alike is that 3D printed materials would meet or exceed the mechanical properties of the equivalent conventional manufacture.

1.1.2 Charpy impact test

The mechanical property, toughness of a material is its ability to undergo large strains prior to fracture when loaded and is directly correlated to the impact energy or

the increase in internal energy. Fracture toughness is important because brittle failure is associated with a rapid propagation of cracking resulting in catastrophic failure. Augustin G.A. Charpy discovered the experimental impact-pendulum test method for measuring the toughness of a material in 1901 [5]. However, it was not until World War II, in which US-built Liberty ships (Fig. 1.1) were appearing to fail prematurely due ductile-to-brittle transition resulting from warm to cold environment, that the Charpy impact test gained significant importance [6].

Fig. 1.1. Fractured Liberty ship located at dock. Extracted from [6].

The impact properties of materials is also critical in determining its performance in high strain rate deformation applications, e.g., ballistics, injection molding, crash-worthiness and blast loading of structures.

1.1.3 Charpy impact test of 3D printed metals

There is limited published data on the impact properties of 3D printed 15-5 stainless steel; especially at cryogenic and high temperatures. Past research has been concentrated mainly on the effects of printing technique, process parameters and printing orientation rather than specimen temperature on the impact energy of 3D printed stainless steel.

Studies on 3D printed 316L stainless steel, which has similar mechanical properties as 3D printed 15-5 stainless steel, at room temperature by Pitrmuc, Z. et al. [7] and Hendrickson, J.W. [8] using the direct metal laser sintering (DMLS) technique indicate an impact energy of 136.0 J/cm^2 for horizontal built and 41.2 J/cm^2 for vertical build respectively. Furthermore, at room temperature, Sistiaga, M. L. M. [9] found the impact energy to be 119.5 J/cm^2 using horizontal build in selective laser sintering (SLS) prepared specimen whereas the the published conventionally manufactured equivalent was 114.0 J/cm^2 [10]. Hence, even if the printing orientation was not investigated in this study, the predicted impact energy of horizontal-build 3D printed (DMLS) 15-5 stainless steel is expected to be approximately three times that of vertical-build.

In this study, the impact properties of horizontal-build 3D printed (DMLS) of 15-5 stainless steel were investigated at low temperature (77 K), room temperature (298 K) and high temperature (723 K) using a combined experimental and numerical modeling approach. The impact properties include the impact energy which correlates to toughness (area under the stress versus strain curve), microsurface investigation and visual inspection of fractured surface in the Charpy impact test. Numerical modeling was to performed to corroborate the results of the experimental Charpy impact test such that a model can be properly calibrated to provide an effective alternative to the experimental testing as the impact properties can be investigated at numerous testing temperatures with minimal cost and effort.

1.1.4 Ballistic impact simulations

A ballistic impact simulation was performed as a qualitative analysis of a 3D printed (DMLS) 15-5 stainless steel plate to determine the real-life application of the material and to also compare against the experimental and numerical simulations of the Charpy impact test to determine if there are any trends in its behavior at high strain rate impact i.e. 300 m/s. Hence, experimental ballistic impact testing was not included in the scope of this study. Similar temperature and material properties for horizontal-build 3D printed 15-5 stainless steel used in the Charpy impact simulation were adopted for the missile and plate with the specific aim of determining its application in the defense industry.

The impact energy, the effective plastic strain and displacement of a typical plate as well as the exit velocity of a typical missile were investigated in the ballistic impact simulation to determine whether or not the horizontal-build 3D printed (DMLS) 15-5 stainless steel plate can be used in safely dissipating the kinetic energy of a missile.

The eventual outcome of this study is to determine the suitability of 3D printed 15-5 stainless steel in tool making, medicine, military, oil and gas, infrastructure and aerospace industries.

2. CHARPY IMPACT TEST - EXPERIMENTAL PROCEDURE

2.1 Specimen preparation

2.1.1 Chemical composition

The specimens were prepared using 15-5 precipitation hardened (PH) stainless steel fine powder, termed as "EOS Stainless Steel PH1" procured from EOS (EOS GmbH Electro Optical Systems, Germany) [11]. The chemical composition of the powder expressed as percentage by weight is presented in Table 2.1.

Table 2.1.
Chemical composition of 3D printed 15-5 stainless steel [11].

Element	% **by Weight**
Carbon	0.07
Manganese	1.00
Silicon	1.00
Chromium	14.00-15.50
Nickel	3.50-5.50
Copper	2.50-4.50
Molybdenum	0.50
Niobium	0.15-0.45
Iron	Balance

The scanning electron microscopy (SEM) image of the 15-5 stainless steel powder [12] used for the specimen preparation is shown in Fig. 2.1. An average particle size of 20 μm can be observed.

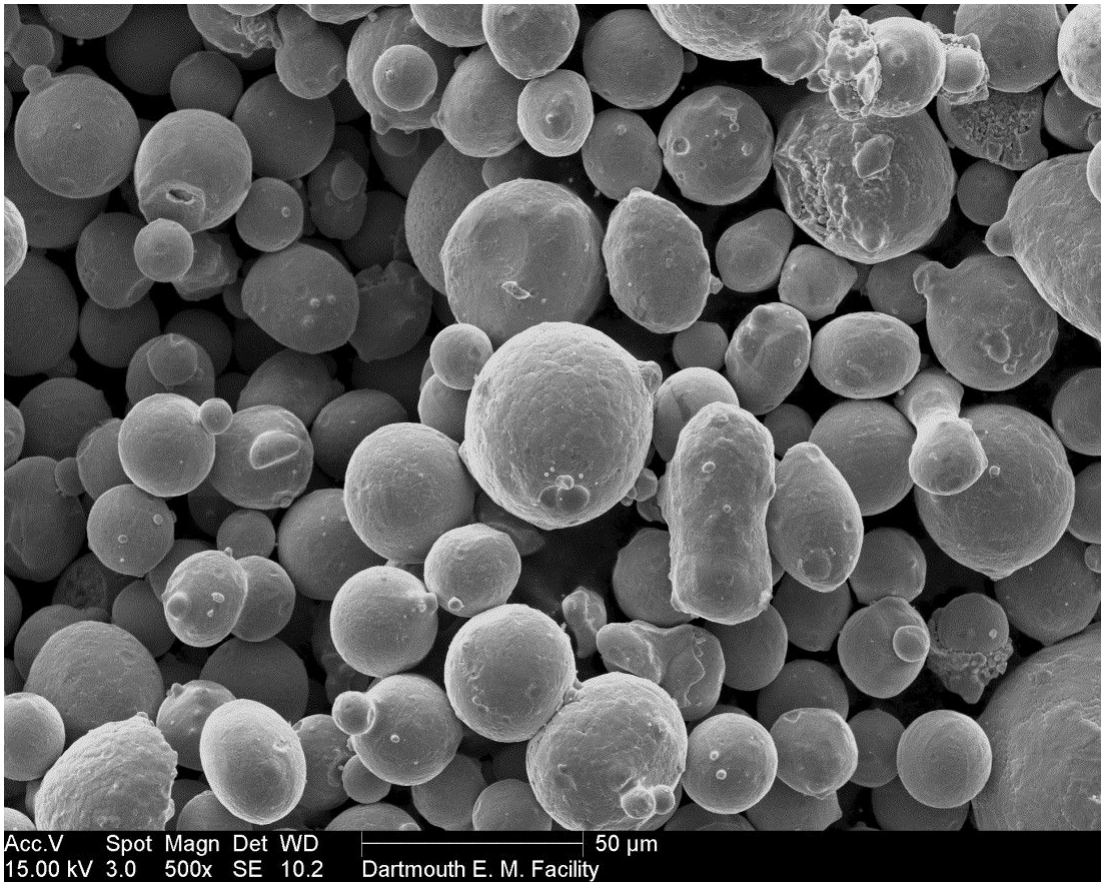

Fig. 2.1. SEM image of EOS 15-5 stainless steel powder [12].

This type of stainless steel is characterized by high corrosion resistance and excellent mechanical properties of precipitation hardened state hence is particularly applicable in the fields of medicine, aerospace, tool making, functional parts and prototypes.

2.1.2 Preparation of STL file for 3D printing

A geometric model was prepared in accordance with the ASTM E23-16b [1] using the Computer Aided Design (CAD) software, PTC Creo Parametric 2.0 [13] and saved as an STL file. The dimensions of the specimen were 10 *mm* x 10 *mm* x 55 *mm* with a 2 *mm* deep, 45 degree centered v-notch and a filleted notch apex of radius of 0.25 *mm* on the long face. Fig. 2.2 illustrates the key dimensions and 3D rendering of the specimen.

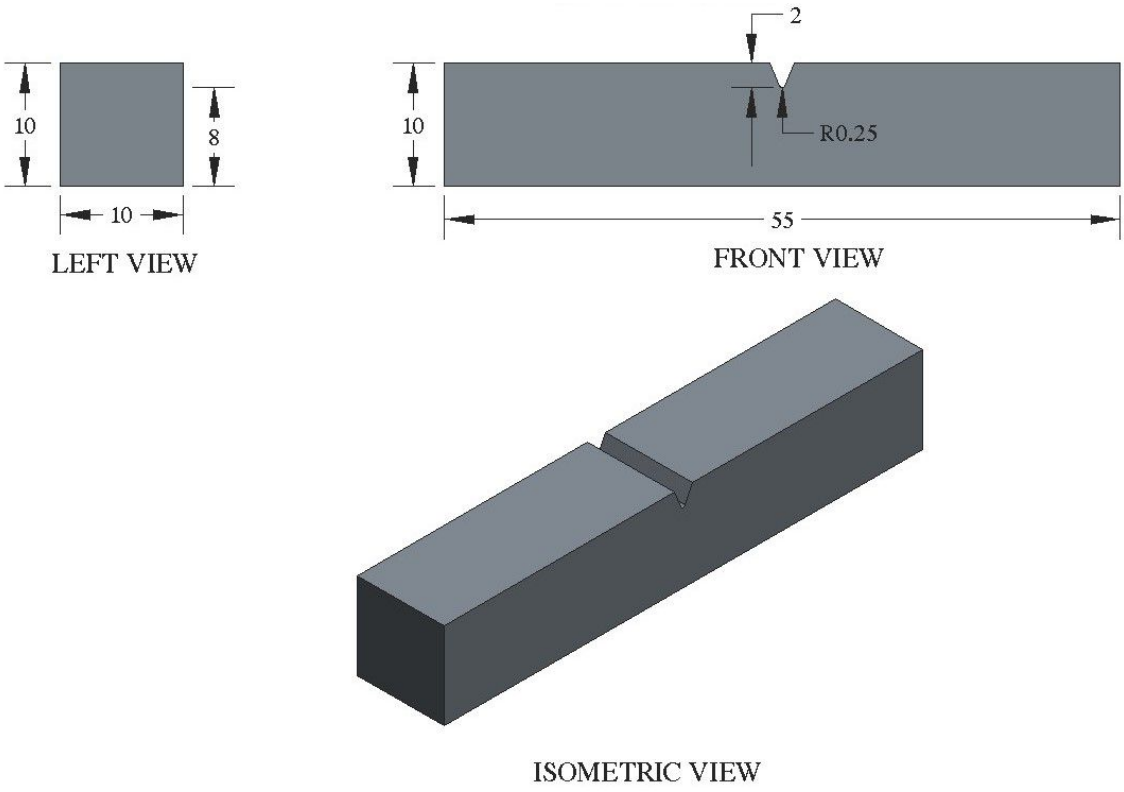

Fig. 2.2. Typical dimensions and 3D rendering of specimen [13] (dimensions in *mm*).

2.1.3 3D printing of specimen

The Charpy impact test specimens were manufactured using the PBF process which involve the DMLS technique in the EOSINT M270 machine (EOS GmbH Electro Optical Systems, Germany) [14] which is equipped with a 200 W single mode Yb fiber laser of 1070 nm wavelength. The process parameters setting include the laser power of 170 W, scan speed of 1250 mm/s in the continuous wavelength mode, a hatch spacing of 100 μm, material layer thickness of 30 μm and a laser beam spot size of $\sim$ 50 μm in diameter [12]. The processing was conducted in an argon environment to prevent oxidation during printing. All specimens were manufactured in the horizontal orientation on the built platform. Fig. 2.3 shows a photograph of the finished 3D printed specimen ready for the Charpy impact test.

Fig. 2.3. 3D printed specimen.

2.1.4 Mechanical smoothening of v-notch

The 2mm deep v-groove in the specimen was formed by printing instead of machining, however, the surface within the groove was jagged, hence was mechanically smoothened using a hand held file followed by manual sanding to ensure that the final geometry was in compliance with the provisions of the ASTM E23-16b [1].

2.1.5 Heat treatment

The heat treatment of the specimens was for the specific purpose of modifying the temperature of each to the desired value and were not intended as a traditional heat treatment such as hot isostatic pressing (HIP), due to the relatively short period of exposure as compared to longer duration-controlled heating and cooling in common heat treatment systems. Hence, for this study, age hardening (which requires the specimen to be subjected to hours of treatment at an elevated temperature) was considered negligible. Age hardening may be considered for longer exposure time as shown in published literature [15] on the properties of 3D printed 15-5 stainless steel using DMLS which indicates a hardness of 25-35 HRC at as-built condition compared to above 40 HRC for age hardened specimens (subjected to an elevated temperature of 763 K maintained for a duration of 6 hours).

Two specimens were prepared for each of the specified temperatures that was measured by an infrared thermometer, resulting in the printing of a total of 6 specimens. Two specimens were subjected to cryogenic temperatures using liquid nitrogen for a period of 10 minutes prior to testing at 77 K. Another two specimens were placed in a furnace and their temperature was raised to 298 K prior to testing and finally the remaining specimens were left in the oven for 15 minutes until their temperature reached 1000 K, then allowed to cooled to the testing temperature of 723 K. An infrared thermometer was used to measure the temperature of each specimen immediately before the Charpy impact test.

2.1.6 Testing procedure

The Charpy impact test was conducted at the Mechanical Engineering Laboratory, Purdue University, West Lafayette using the SATEC SI-1C universal pendulum-impact testing machine shown in Fig. 2.4, supplied by Instron, Grove City, PA [16]. After the specimen was heat treated to the desired temperature, the Charpy impact test was undertaken in accordance with the ASTM E 23-16b [1].

Fig. 2.4. SATEC SI-1C universal pendulum-impact testing machine [16].

For the pendulum-impact tester used in the experiment, the dial gauge measurement represents the energy absorbed by a simply supported notched specimen resulting from a striker of mass m free falling through a distance of h. The theoretical potential energy of the striker, mgh is converted to kinetic energy, $0.5mv^2$ when released by virtue of free fall due to gravity. Upon impact, a fraction of the kinetic energy results in an increase in the internal energy of the specimen. This absorbed energy is correlated to the toughness of the specimen.

In this experiment, the high latch position was adopted; this represents total energy of 406.7 J, considering the 30.24 kg striker was raised at 45 degrees to the 12 o' clock position. Hence given that the diameter of the pendulum was 0.8 m, the total height, h above the specimen was $0.8 + 0.8 * Cosine(45) = 1.366$ m. The specimen

was placed between the two anvils using calipers, and the dial gauge was reset to the zero position, followed by the release of the striker from the rest position. Following the breaking of the specimen, the impact energy was measured on the gauge and recorded.

The temperature of the broken specimen was remeasured for assurance of specified testing condition. Finally, the brake was applied to ensure that the pendulum returned to its stable hanging position.

This procedure was repeated for each of the specimens.

3. CHARPY IMPACT TEST - NUMERICAL MODELING

3.1 Geometry

Similar to the specimen described in Section 2.1 of this report, the main geometry of the striker and anvil was adopted from the ASTM E23-16b [1] standard. The CAD model of the striker and anvil were created in the geometrical modeling software PTC Creo Parametric 2.0 [13] and saved as .iges files. Drawings of the striker and anvil are presented in Fig. 3.1 and Fig. 3.2 respectively.

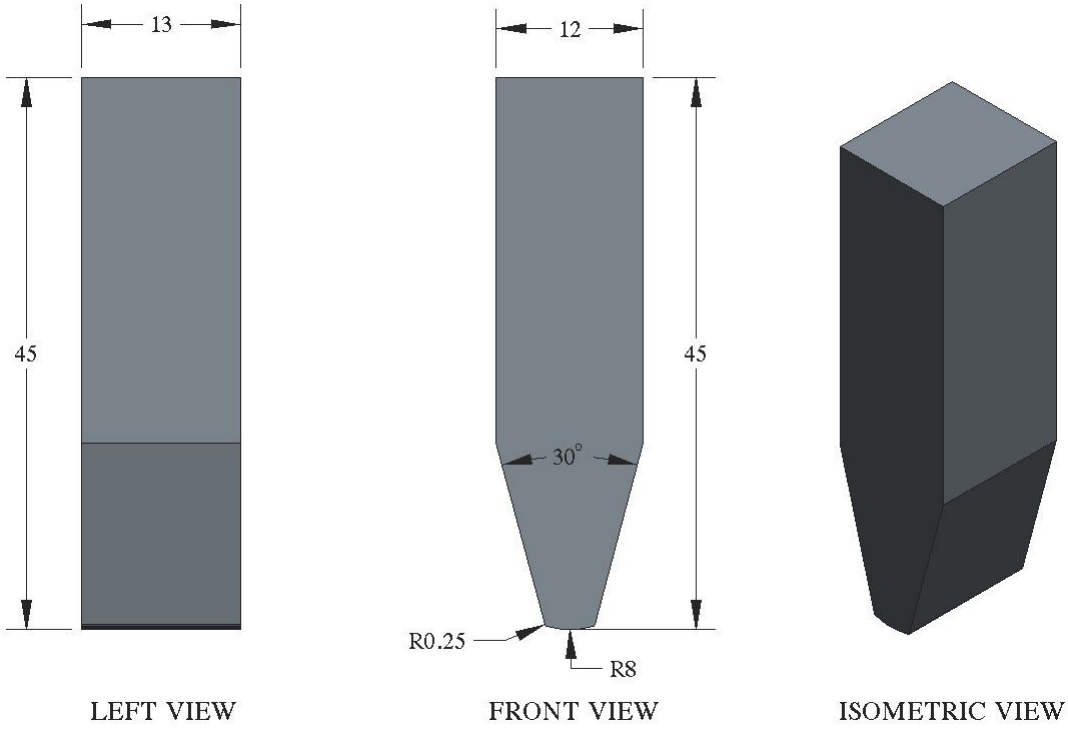

Fig. 3.1. Drawing of striker in PTC Creo Parametric 2.0 [13] (dimensions in *mm*).

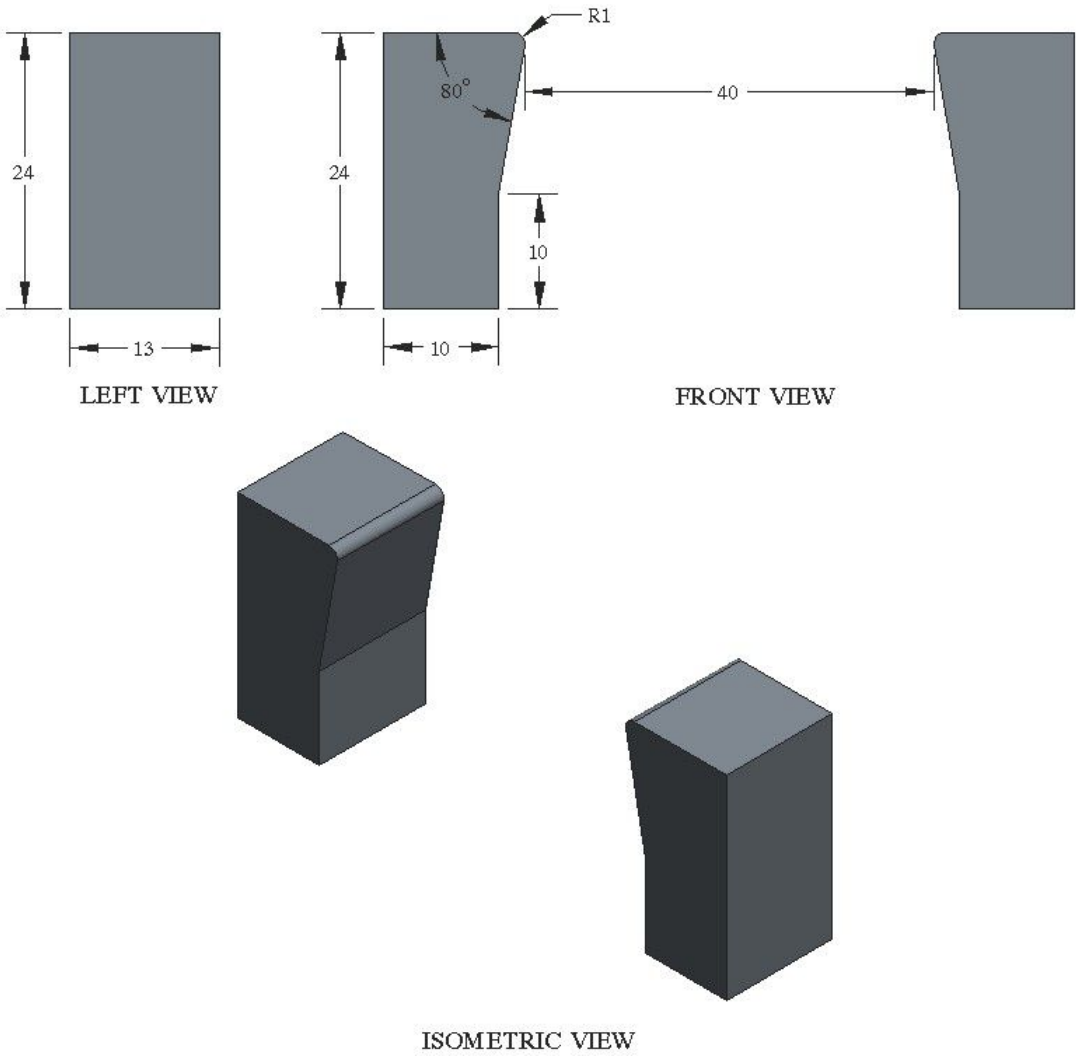

Fig. 3.2. Drawing of anvil in PTC Creo Parametric 2.0 [13] (dimensions in mm).

3.2 Modeling software

LS-PREPOST [17], a software that is free for download and use was selected for modeling geometry, meshing, velocity, boundary condition and material assignment. This information was written in a keyword or .k file. The keyword file consists of an array of named columns of data that represents each of the model features.

3.3 Finite element mesh

The .iges file consisting of the striker, specimen and anvil parts were imported into LS-PREPOST [17]. Brick solid elements were used for all the imported parts with further mesh refinement on the specimen, primarily at the impact zone as shown in Fig. 3.3.

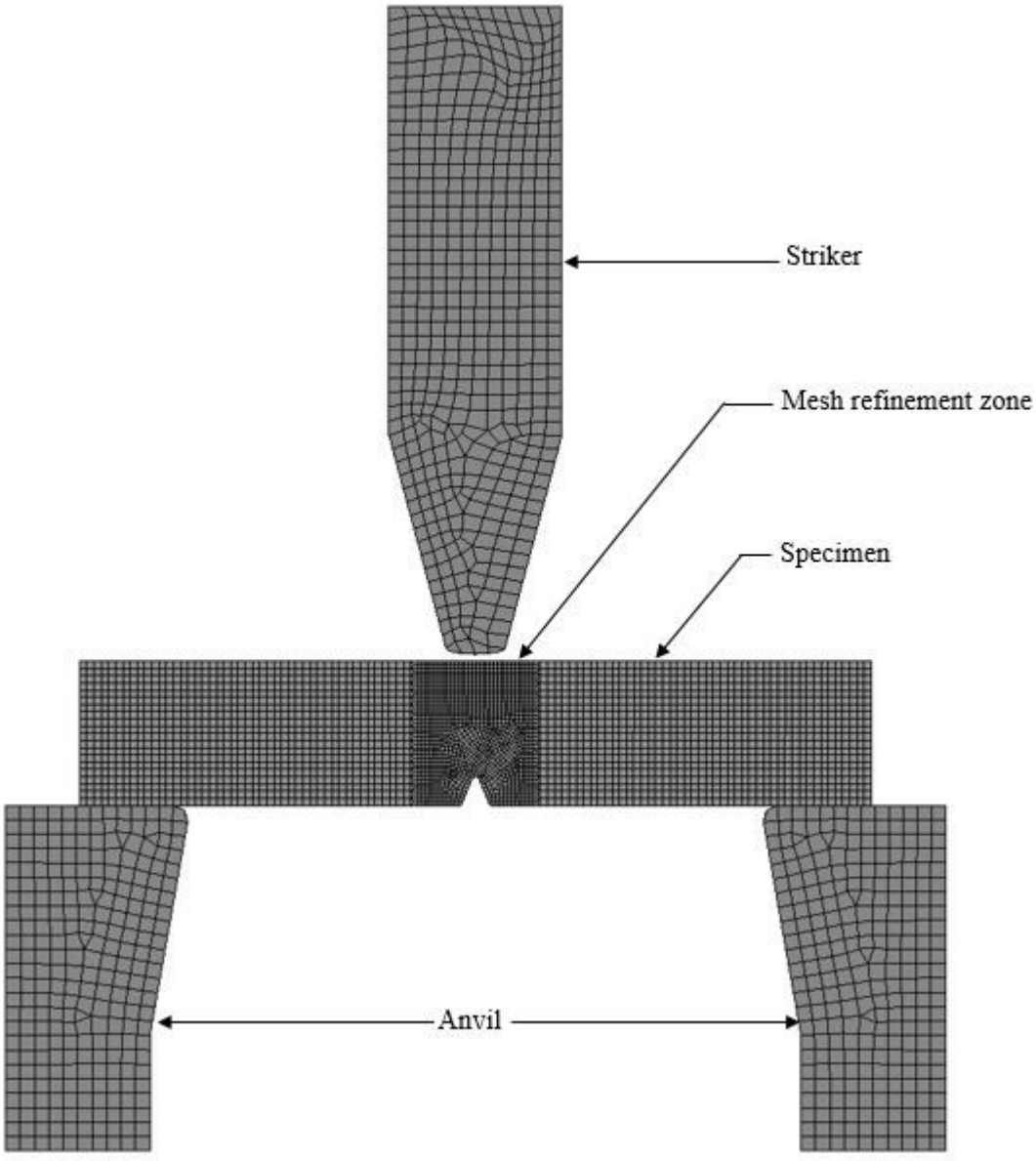

Fig. 3.3. Finite element mesh of striker, specimen and anvil in LS-PREPOST [17].

The mesh refinement was undertaken by creating a shell element out of a solid face (side), followed by splitting/dividing the mesh within the impact zone. Triangular meshes were created to connect the larger mesh with the refined zone. A solid mesh was achieved by shell dragging through a compartmentalized extrusion through the thickness of the specimen. Brick solid mesh was used in preference to tetrahedral mesh because of better accuracy per mesh size for high strain rate application. Some tetra mesh types exhibit volumetric locking which results in a more rigid response, further refinement result in increased accuracy with the consequence of higher demand for computing resources, hence was not considered.

The distance between the striker and specimen was assigned a relatively close distance i.e. 1.0 mm in order to reduce analysis time.

3.4 Material model

3.4.1 Johnson-Cook constitutive model

In order to capture the effects of high strain rate and adiabatic heating during impact, the Johnson-Cook (J-C) constitutive model [18] was assigned to the specimen in LS-PREPOST [17] using the *Mat_015 material selection input. The J-C phenomenological flow stress model is not based on traditional plasticity theory, rather, it consists of a strain hardening component (first expression), strain-rate component (second expression) and a thermal softening component (third expression) in a multiplicative manner as shown in Eq. (3.1):

$$\sigma_{eff} = \left(A + B\overline{\varepsilon}^{p^n}\right)\left[1 + C\ln\left(\frac{\dot{\overline{\varepsilon}}^p}{\dot{\varepsilon}_0}\right)\right]\left[1 - \left(\frac{T - T_r}{T_{melt} - T_r}\right)^m\right] \tag{3.1}$$

Where the parameters are defined as follows: σ_{eff} effective stress, $\overline{\varepsilon}^p$ effective plastic strain, $\left(\frac{\dot{\overline{\varepsilon}}^p}{\dot{\varepsilon}_0}\right)$ dimensionless strain rate where $\dot{\varepsilon}_0$ and $\dot{\overline{\varepsilon}}^p$ represent reference and effective plastic strain rates respectively, and $\left(\frac{T-T_r}{T_{melt}-T_r}\right)$ the dimensionless homologous temperature, in which, T, T_r and T_{melt} represent the initial, reference and melting temperatures respectively.

The J-C constitutive model parameters, A plastic yield stress, B plastic hardening parameter, n plastic hardening exponent, C strain rate coefficient and m temperature softening exponent are all experimentally and numerically determined.

The temperature softening expression shown in Eq. (3.1), represents the effect on flow stress due to the adiabatic condition caused by plastic work of deformation. The reference temperature, T_r represents the temperature of the specimen prior to testing i.e. 77 K, 298 K and 723 K, whereas the initial temperature, T represents the temperature after impact and is due to adiabatic heating. The maximum reference temperature, T_r was chosen to be significantly lower than the melting temperature, T_{melt} of the specimen, because of the uncertainty of its impact behavior in the experimental Charpy impact test as well as the accuracy of the J-C constitutive model at near-melting point.

Since the J-C constitutive material model for 3D printed 15-5 stainless steel parameters were not readily available, the wrought equivalent [19] were used in this study and are presented in Table 3.1. The values of A, B, n, C and m were each investigated for T_r values of 77 K, 298 K and 723 K using numerical modeling to match the behavior of the experimental Charpy impact test; however, the effect of each constitutive model parameter on the impact energy was found to be negligible. More accurate values of each parameter may be explored using the torsion test, dynamic Hopkinson bar test and tensile tests over a range of temperatures [18]. Consistent with the experimental Charpy impact test, the reference values for low, room and high temperatures were assigned for T_r for each of the simulation.

Table 3.1.
Johnson-Cook constitutive model parameters for 3D printed 15-5 stainless steel [19].

J-C model parameter used in Eq. (3.1)	**Value**
A	855 MPa
B	448 MPa
n	0.140
C	0.014
m	0.63
$\dot{\varepsilon}_0$	1.0 s^{-1}
T_{melt}	1713 K
T_r (77 K)	77 K
T_r (298 K)	298 K
T_r (723 K)	723 K

3.4.2 Johnson-Cook fracture model

In order to model the failure characteristics beyond plastic deformation, the Johnson-Cook (J-C) fracture criteria [20] was used in the *Mat_015 material model of LS-PREPOST [17]. Fracture occurs when the following fracture parameter, D, reaches unity as shown in Eq. 3.2:

$$D = \sum \frac{\Delta \overline{\varepsilon}^p}{\varepsilon^f} \tag{3.2}$$

Where $\Delta \overline{\varepsilon}^p$ is small increment of equivalent plastic strain, and ε^f is equivalent strain at failure under given conditions defined by Eq. 3.3:

$$\varepsilon_f = \left[D_1 + D_2 \exp D_3 \left(\frac{p}{\sigma_{eff}}\right)\right] \left[1 + D_4 \ln \left(\frac{\dot{\overline{\varepsilon}}^p}{\dot{\varepsilon}_0}\right)\right] \left[1 + D_5 \left(\frac{T - T_r}{T_{melt} - T_r}\right)\right] \tag{3.3}$$

Where: $\left(\frac{p}{\sigma_{eff}}\right)$ triaxiality ratio where p is the hydrostatic pressure. The J-C fracture model parameters, D_1 initial failure stress, D_2 exponential factor, D_3 triax-

ility factor, D_4 strain rate factor and D_5 temperature factor are all experimentally and numerically derived from the torsion test over a range of strain rates, dynamic Hopkinson bar test over a series of temperatures and quasi-static tensile test over an assortment of notched specimens [20].

The J-C fracture model parameters, $D_1 \sim D_3$ for 3D printed 15-5 stainless steel were extracted from published literature [21]. The fracture parameters D_4 and D_5 were obtained from [20] given the similar fracture mechanism as AISI 4340 steel.

For T_r values of 77 K, 298 K and 723 K, each fracture parameter was investigated whilst keeping the other parameters as well as the J-C constitutive model parameters constant in the numerical modeling iterations. This approach enabled the determination of the critical J-C fracture parameters that resulted in the convergence of the numerical modeling with the experimental Charpy impact test.

The numerical modeling iterations indicated that the impact energy was mostly affected by D_1 whilst keeping the J-C constitutive model and fracture parameters $D_2 \sim D_5$ constant. The optimized values of D_1 corresponding to T_r values of 77 K, 298 K and 723 K were -0.600, -0.193 and -0.143 respectively as shown in Table 3.2.

Table 3.2.
Fracture parameters for 3D printed 15-5 stainless steel.

J-C model parameter used in Eq. (3.3)	**Value [Ref.]**
$D_1(77K)$	-0.600
$D_1(298K)$	-0.193
$D_1(723K)$	-0.143
D_2	3.810 [21]
D_3	-1.847 [21]
D_4	0.002 [20]
D_5	0.610 [20]

Further reduction in the value D_1 at 77 K during the numerical modeling iterations did not result in a significant change in the impact energy, hence the threshold value of -0.600 was adopted.

3.4.3 Equation of state

The Johnson-Cook constitutive model requires an equation of state for representing the behavior of the impacted material, hence a simple linear polynomial equation of state input was provided in LS-PREPOST [17]. To activate the material model, the bulk modulus, C_1 (169.1 GPa) was populated in the input card whilst $C_2 \sim C_5$ were all set to zero. Given that the initial temperature, T is equal to the reference temperature, T_r during testing, the initial internal energy in the input card was set to zero.

3.4.4 Physical and mechanical properties

The physical and mechanical properties of 3D printed 15-5 stainless steel adopted from [19] are shown in Table 3.3.

Table 3.3.
Physical and mechanical properties of 3D printed 15-5 stainless steel [19].

Material Property	**Value**
Density, ρ	7850 kgm^{-3}
Young's Modulus, E	212 GPa
Poisson's Ratio, ν	0.291
Shear Modulus, G	149.5 GPa

3.4.5 Modified density of striker

In order to reduce computing effort, part of the geometry of the striker was reduced whilst maintaining the relevant impact section geometry in accordance with the ASTM E23-16b [1]. Given that the mass of the striker used in the Charpy impact experiment was 30.24 kg, adjustment of the density based on the revised geometry was necessary to preserve mass. The volume of the striker as shown in Fig. 3.4 is 6212.99 mm^3 as extracted from Creo Parametric 2.0 [13].

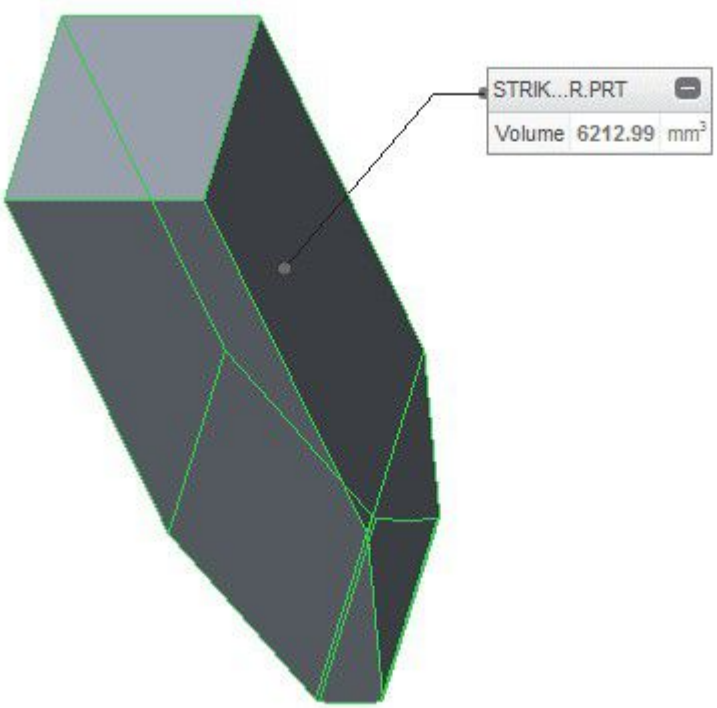

Fig. 3.4. Volume of striker extracted from Creo Parametric 2.0 [13].

Hence the adjusted density of the striker that ensures that the mass is consistent with the experimental condition is $4.87e^{-3}$ $kgmm^{-3}$.

3.4.6 Initial velocity of striker

The total energy of the striker at any position is the sum of potential energy and kinetic energy, i.e., $mgh + 0.5mv^2$, where m is the mass of striker, g is acceleration due to gravity, h is the height of the initial position of striker, and v is the velocity. Upon impact with the specimen, by virtue of the principle of conservation of energy, the potential energy is equivalent to the kinetic energy. The initial velocity was computed by the cancellation of mass on both sides of the equation resulting in the velocity being a function of the height only i.e. $v = \sqrt{2gh}$. Where the height, h was determined from the experimental Charpy impact test i.e. 1.366 m, the acceleration due to gravity is taken as 9.81 ms^{-2} and the corresponding calculated initial velocity was 5.18 ms^{-1}. An illustration of the assigned velocity is shown in Fig. 3.5.

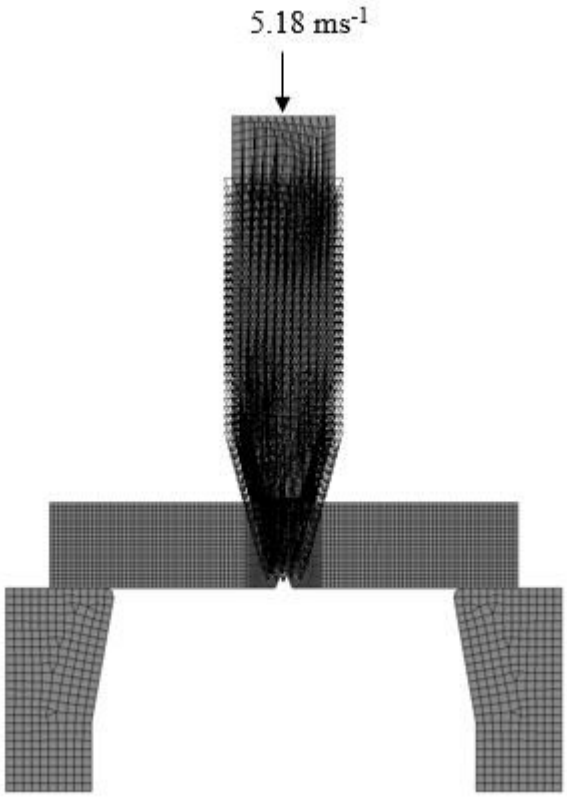

Fig. 3.5. Initial velocity of striker.

3.4.7 Rigid body assignment

The striker and anvil were assigned rigid body properties as shown in Fig. 3.6 to simulate experimental test conditions and to mitigate against energy loss in the system.

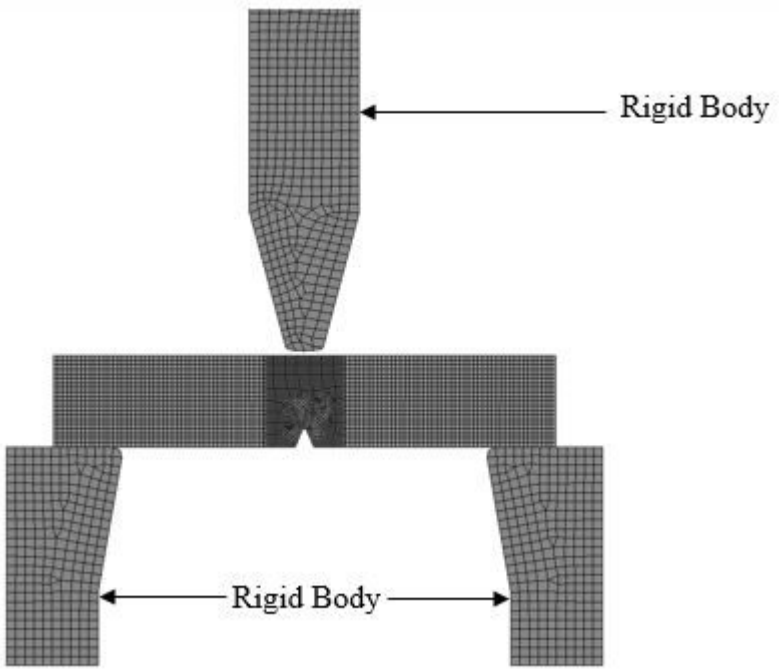

Fig. 3.6. Rigid body assignment to striker and anvil.

3.4.8 Boundary conditions

Sliding contact conditions were assigned to the specimen and anvil interface as shown in Fig. 3.7 and striker and specimen interface as shown in Fig. 3.8. Sliding contact were used in order to reduce the energy dissipated through interface friction that would result in reduced impact energy.

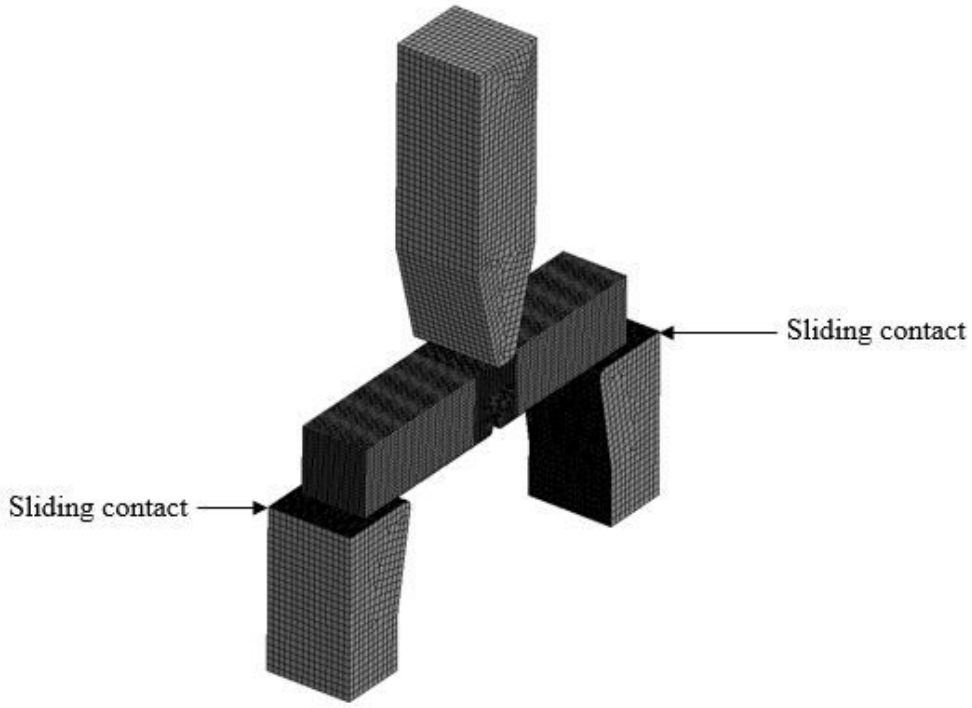

Fig. 3.7. Sliding contact assignment between specimen and anvil.

3.4.9 Analysis software

The LS-PREPOST [17] keyword (.k) files for each temperature were used in the structural analysis software, LS-DYNA [22] for the numerical modeling of the Charpy impact test and ballistic impact simulation. The analyses were conducted using the supercomputer available through Karst, an integral part of the University Information Technological Services (UITS) housed in the IU Bloomington Data Center, Indiana. The LS-DYNA [22] version ls971s R4.2.1 and revision 53450 software package used in this study was licensed to Indiana University-Purdue University Indianapolis (IUPUI) from the Livermore Software Technology Corporation (LSTC). The Intel Fortran 10.1 compiler, Xeon64 platform and an Linux 2.6.2018 operating system were used.

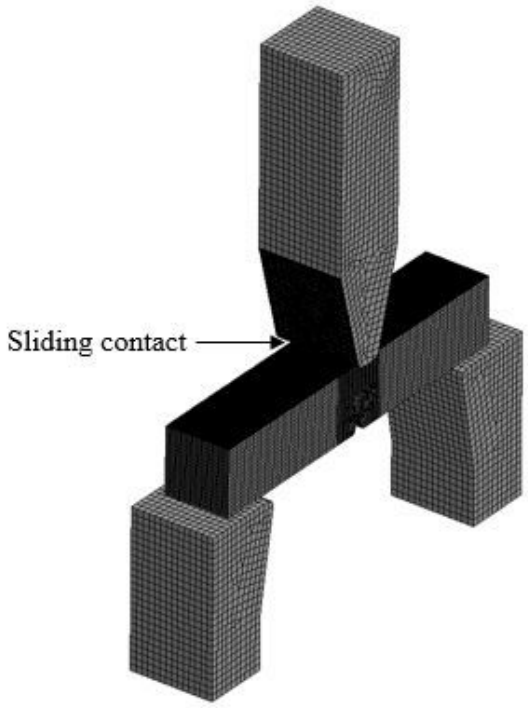

Fig. 3.8. Sliding contact assignment between striker and specimen.

3.4.10 Supercomputer hardware

Karst comprises 228 general-access compute nodes, 28 condominium nodes, and 16 dedicated data nodes (for separate handling of data-intensive operations). Each node has an IBM NeXtScale nx360 M4 server equipped with two Intel Xeon E5-2650 v2 8-core processors (Xeon64 systems). Each data node has 64 GB of RAM and 24 TB of local storage. The supercomputer is outfitted with 32 GB of RAM and 250 GB of local disk storage. The memory required to begin solution was 14.59 GB and additional dynamically allocated memory was 9.55 GB resulting in a resulting total of 24.15 GB.

3.4.11 Timestep and simulation time

The timestep and simulation time were 1.92351E-08 s and 6265 s respectively.

4. BALLISTIC IMPACT SIMULATION

4.1 Overview

Ballistic impact modeling of 3D printed 15-5 stainless steel was performed to investigate its applicability in defense using the impact energy, maximum effective plastic strain and deformation of a fixed plate as well as the exit velocity of a typical missile.

4.2 Geometry

A typical 9.0 mm diameter, 45 mm long missile and 1.5 mm thick, 150 mm wide square sheet were chosen for the ballistic impact study. Due to the difficulty in trimming and modifying a curved surface in preparation of sweep volume solid meshing for an IGES file generated from a Creo Parametric 2.0 [13] file, a workable geometric model was prepared in Dassault Systmes Solidworks 2017 [23]. Details of the missile and plate are presented in Fig. 4.1.

The techniques used to improve the CAD model in Creo Parametric [13] were adjusting the precision, manipulating the surface at the tip and minimizing the curvature; however persistent errors occurred when determining a sweepable volume for solid meshing, hence the reason for switching the geometrical modeling software packages.

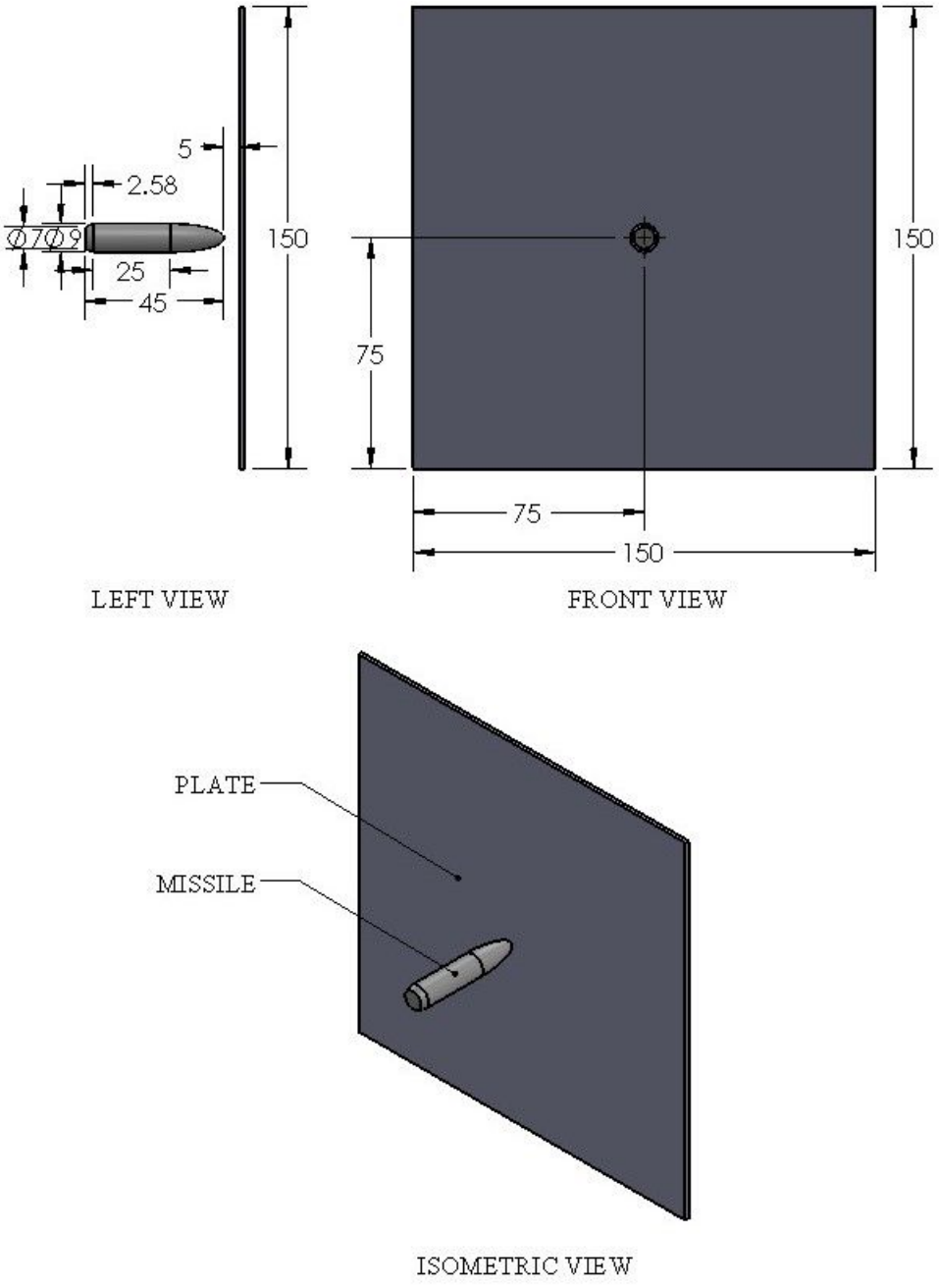

Fig. 4.1. Drawings of missile and plate in Solidworks 2017 [23] (Dimensions in mm).

4.3 Meshing

Brick solid elements were used to model both the missile and plate. Due to the presence of multiple sweep volume in the missile, it was compartmentalized by trimming into individual sweep volume and meshed independently. This was followed by mesh merging, element duplicate merging and reflecting. Finally, a single part was created by transferring the individual solid meshed parts. Automatic brick mesh was selected for the plate, this was followed by further mesh refinement at the impact zone using a combination of triangular and square meshes as shown in Fig.4.2 .

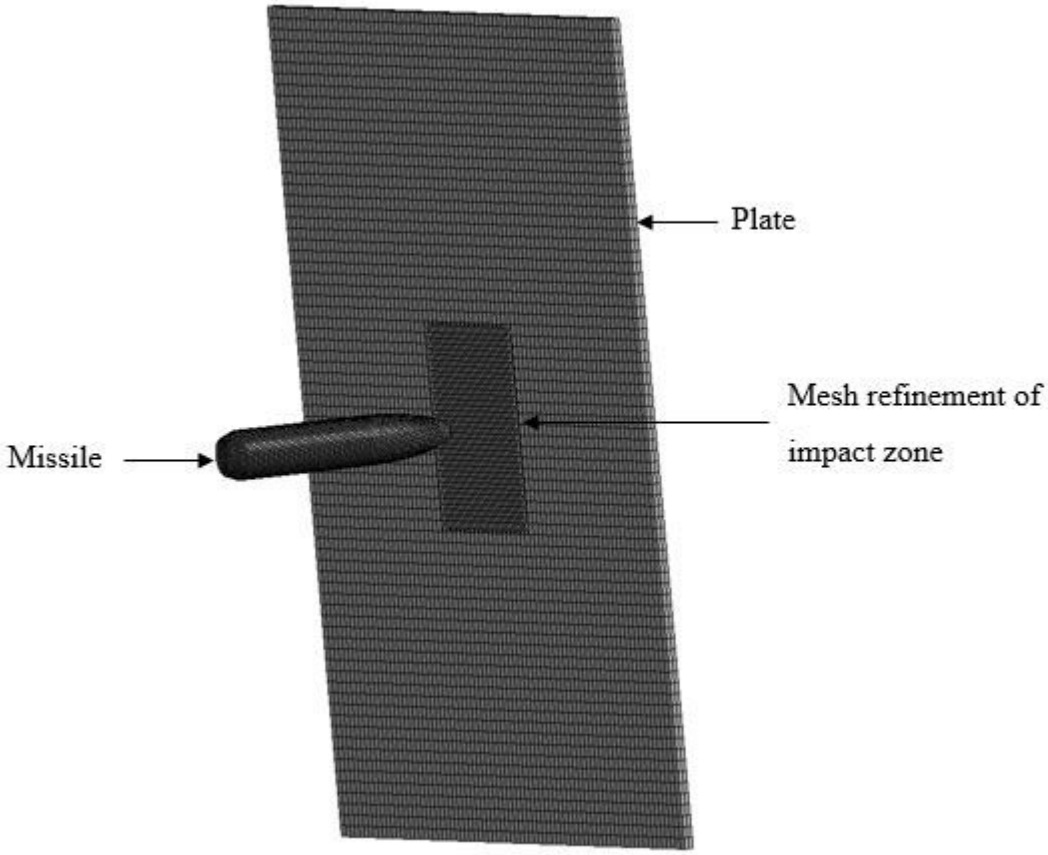

Fig. 4.2. Finite element mesh of missile and plate in LS-PREPOST [17].

4.4 Initial velocity of missile

An initial velocity of 300 ms^{-1} based on similar impact studies [24] for typical rifles was assigned to the missile as shown in Fig. 4.3.

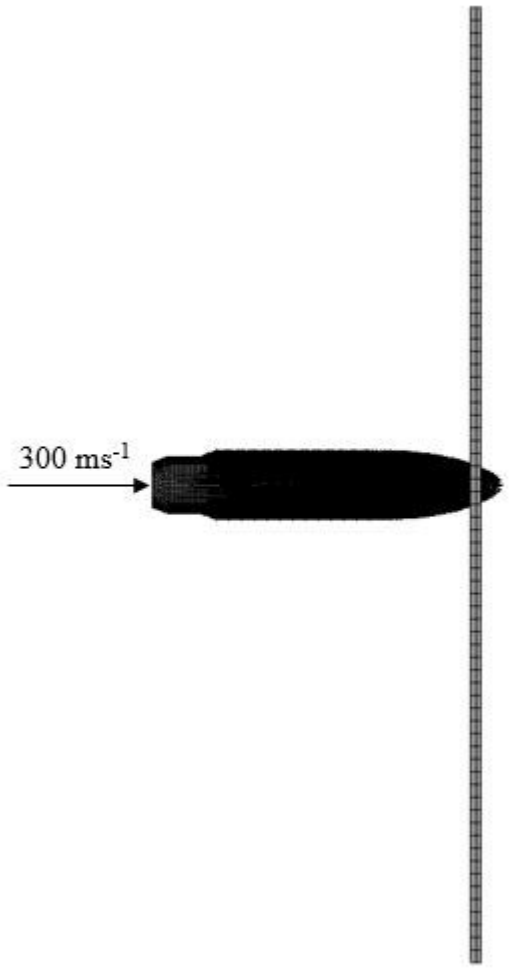

Fig. 4.3. Initial velocity assigned to missile.

4.5 Boundary condition

Fixed boundary conditions were assigned to the edges of the plate as shown in Fig. 4.4. This simplification of the support conditions was necessary to represent a plated section of a defense system for simulation purposes. Actual conditions may

vary based on the geometric configurations of the plate, however was not included in this study.

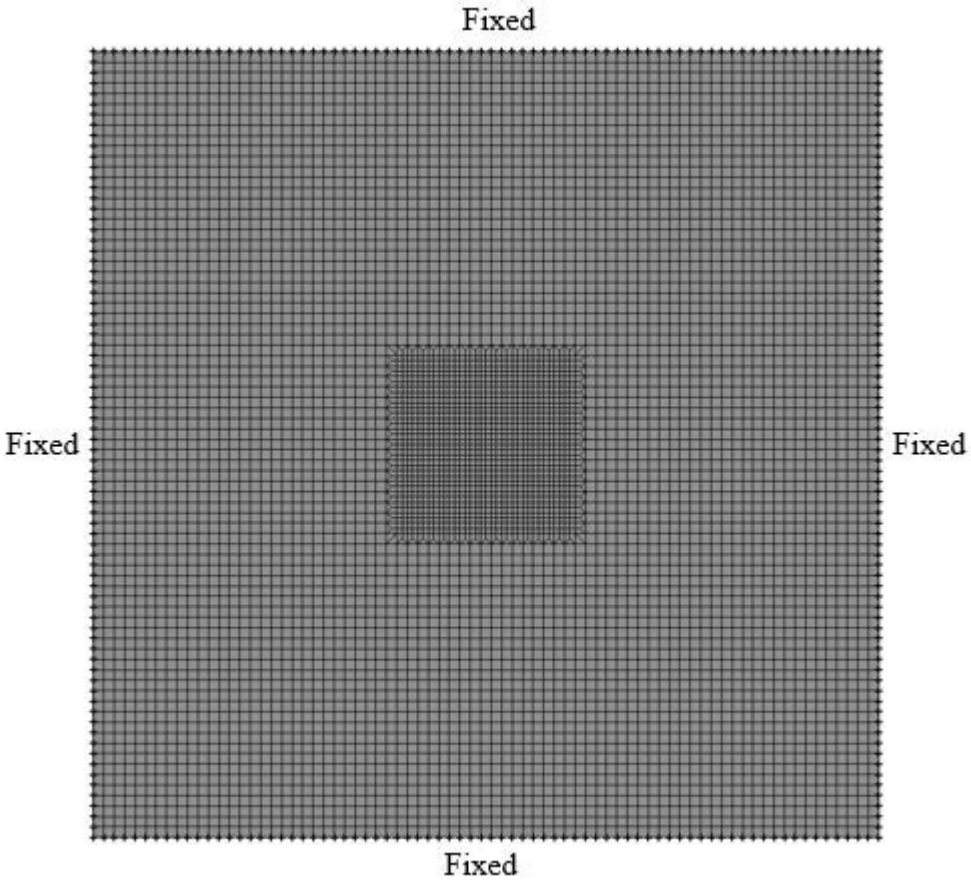

Fig. 4.4. Fixed boundary conditions assigned to plate edges.

4.6 Material model, equation of state and mechanical/physical properties

The input for material model, equation of state and mechanical and physical properties were repeated from Sections 3.1, Section 3.2 and Section 3.3 corresponding to the temperatures of 77 K, 298 K and 723 K for the plate. However, the missile was assigned room temperature properties (298 K) to represent a control that is consistent for all three plate temperatures.

5. RESULTS AND DISCUSSION

5.1 Charpy impact test

During impact testing, one of the specimens at room temperature broke prematurely, resulting in zero impact energy recorded. In addition, one of the high temperature specimens was observed to be 45 K lower than the correct testing temperature of 460 k. These specimens were subsequently removed from the recording of the experiment. The consistency of testing for all three temperatures was maintained by recording a single test result in each of the temperature categories.

5.2 Microstructures of the printed samples at various temperatures

Prior to the Charpy impact testing, microstructures of the specimen cross-sections were characterized using optical microscopy (OM) and SEM. Different temperatures affect the microstructure and the mechanical properties of the stainless steel including its ductility and fracture toughness. The optical microscopic images of three samples at 77 K, 298 K and 723 K are shown in Fig. 5.1. All of the three samples indicate dense microstructure with high relative densities (>99%), with very few pores. The surface textures of room temperature and low temperature samples are very similar, except that the room temperature one has a few visible pores (Fig. 5.1(b)). When heat treated at high temperature, large grains are formed (Fig. 5.1(c)), an indication of grain growth at high temperatures.

The high temperature heat treatment acted as an annealing process, so that the crystal lattice may relax and a more ordered grain pattern is formed.

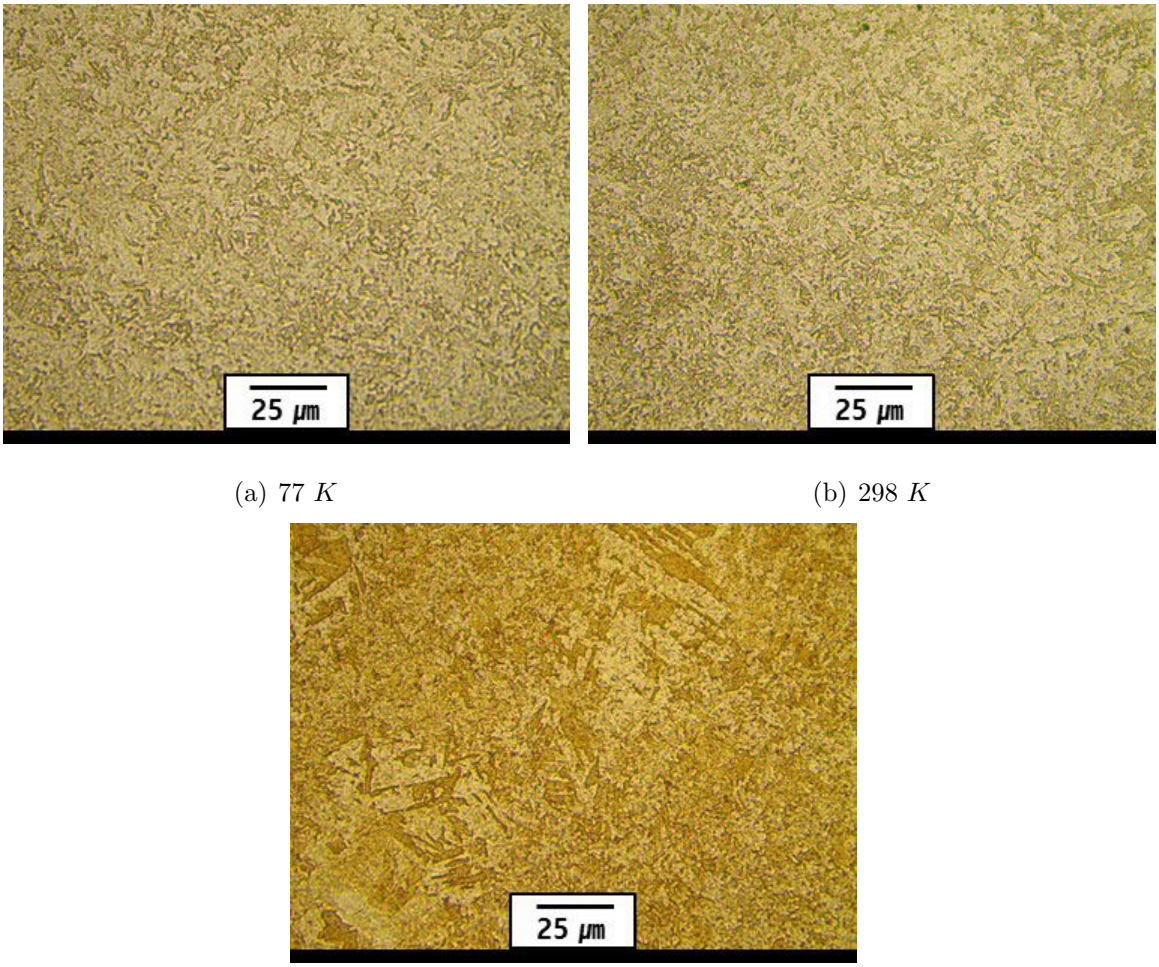

(a) 77 K (b) 298 K

(c) 723 K

Fig. 5.1. OM images(500x magnification) of cross-sections of 3D printed 15-5 stainless steel.

Detailed microstructures are revealed by the SEM images as shown in Fig. 5.2. At room temperature (Fig. 5.2(b)), irregular shaped lack-of-fusion pores are observed due to the insufficient heating by laser source during DMLS process. When the as-printed sample is subjected to furnace heat treatment, the high temperature acts in two ways: increase material diffusion rate and lead to thermal expansion. The surface of the high temperature sample (Fig. 5.2(c)) is smoother, which indicates that the rough surface is flattened by material diffusion at high temperatures. On the other hand, due to the thermal expansion, the compressed materials near the

pore move toward the pore centers, which makes the pore size smaller, and the pore becomes to be circular. At low temperature, because the diffusion rate is much lower, the structural change is minimum, therefore the configuration is similar to the room temperature.

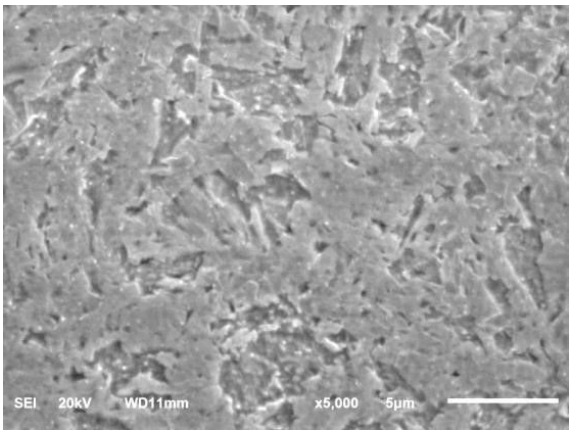

(a) 77 K

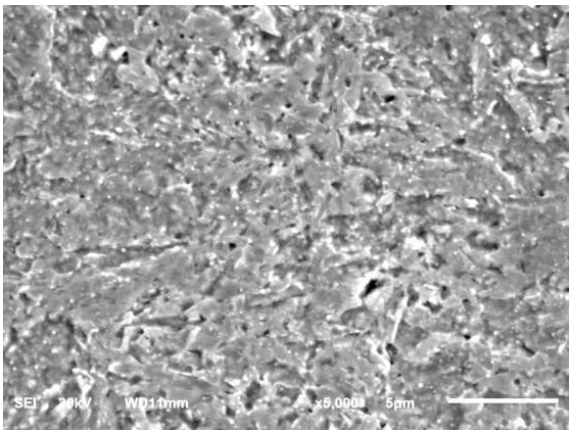

(b) 298 K

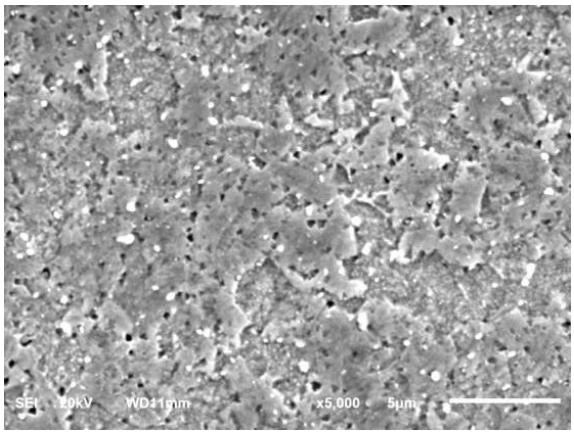

(c) 723 K

Fig. 5.2. SEM images (5000x) of cross-sections (Scale bars represents 5 μm).

In addition to cross-sectional micrographic analysis, the element composition of samples at three different temperatures were determined using energy-dispersive X-Ray spectroscopy (EDX) to corroborate the chemical compositions of the supplied powder. The measured element distributions of the three temperatures are shown in Table 5.1. Although they were tested under different temperature, the element

compositions are almost identical with very slightly difference. For all the three cases, Fe (75.85%-76.06%), Cr (14.80%-14.82%), Ni (4.204.31%), and Cu (3.50%-3.53%) are the four major elements, Si and Nb are two minor elements that have about 1% weight percentage in total. The element weight percentages were not sensitive to temperature in this study.

Table 5.1.
Elements in the 3D printed 15-5 stainless steel samples using EDX.

Element	**Weight percentage (%)**		
	77 K	**298** K	**723** K
Si	0.68	0.65	0.60
Cr	14.80	14.82	14.81
Fe	75.85	76.06	75.88
Ni	4.31	4.20	4.27
Cu	3.53	3.51	3.50
Nb	0.60	0.59	0.72

5.3 Fracture surfaces after Charpy impact test

5.3.1 Microstructure analysis of the fracture surface

After the Charpy impact test, the microstructures of the fracture surfaces were analyzed to investigate the fracture mechanisms and the material behavior under impact loading. The fracture surface micrographs of the low temperature sample are shown in Fig. 5.3. During the impact test, in the fracture region, the direction of tensile stress is normal to the fracture surface. The flat fracture surface in Fig. 5.3 shows that the fracture propagation direction is nearly perpendicular to the tensile direction, which is an indicator of brittle fracture. Almost no plastic deformation can be observed, and the cracks are mostly propagated by cleavage. The fracture

surface includes both transgranular crack thorough grains, and intergranular crack along grain boundaries. The recorded impact energy at low temperature is close to 0 J/cm^2. Such a low toughness means that temperature 77 K is below the ductile-brittle transition temperature for the material. The movement of nearby atoms in the crystal lattice is suppressed by the low temperature, so that long cracks can form easily, resulting in a brittle fracture behavior.

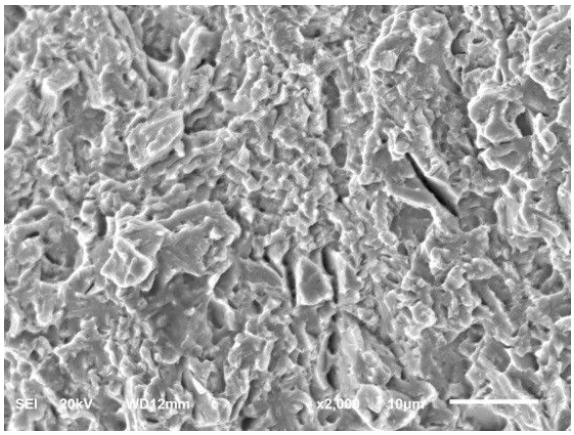

(a) 77 K

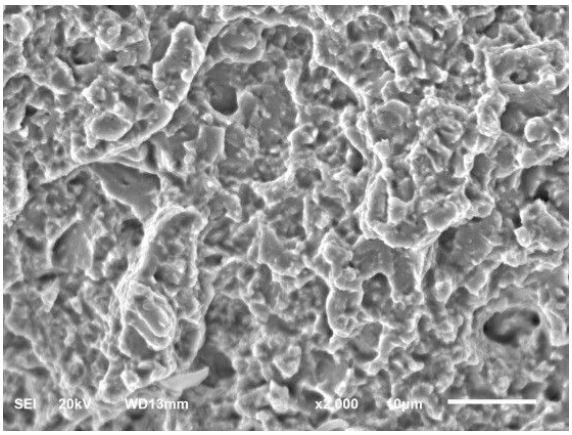

(b) 298 K

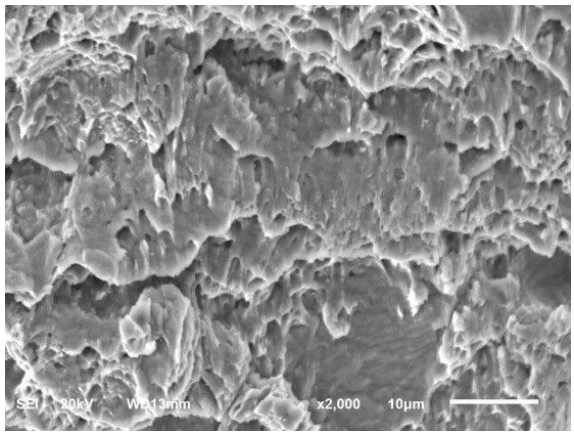

(c) 723 K

Fig. 5.3. SEM images of fractured 3D printed 15-5 stainless steel samples (2000x magnification, scale bar represents 10 μm).

Fig. 5.3(b) shows the fracture surface microstructure of the sample tested at room temperature (298 K). Similar to the low temperature specimen, almost no plastic deformation can be visualized. Intergranular crack along grain boundaries is the dominant fracture mechanism, and a few transgranular crack evidence can be found. This is the main difference from the low temperature fracture, where both transgranular and intergranular crack contribute to the fracture. At room temperature, the tested impact energy is 6.78±4.07 J/cm^2. Although it is still brittle fracture at room temperature, the higher temperature increases the mobility of the lattice, and long cracks propagation is partially suppressed. Therefore the impact energy is higher than that of low temperature.

5.3.2 Comparison between experimental and modeling fracture surface

The fracture surface of the broken specimens were visually inspected to investigate the failure behavior upon impact. The fracture surface at 77 K was almost linear as shown in Fig. 5.4 indicating shear or brittle failure as the striker moves through the specimen. In addition, the maximum effective plastic strain of 0.451 m/m concentrated only at the impact point and along the fracture surface was observed.

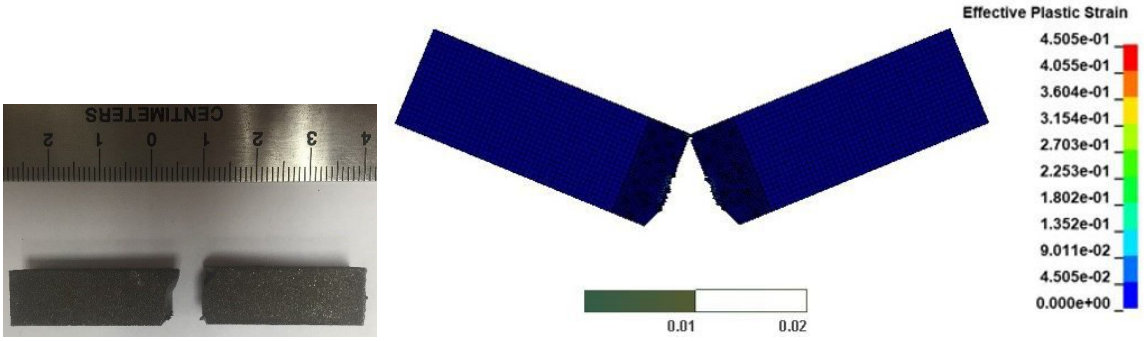

(a) Experimental (b) FEA simulation

Fig. 5.4. Fracture surface and effective plastic strain at 77 K.

Hence, based on this qualitative assessment of both the experimental and numerical modeling fracture surface and effective plastic strain, the most brittle of all specimens was observed at 77 K.

There is a brittle failure of the specimen at 298 K (shown in Fig. 5.5) but the fracture surface is not linear as the 77 K specimen, indicating that there has been an increase in ductility. The maximum effective plastic strain of 0.721 m/m is higher than the value at 77 K but lower than that at 723 K. Hence based on the fracture surface and effective plastic strain, this specimen exhibited higher ductility than the 77 K specimen but lower ductility than the 723 K specimen.

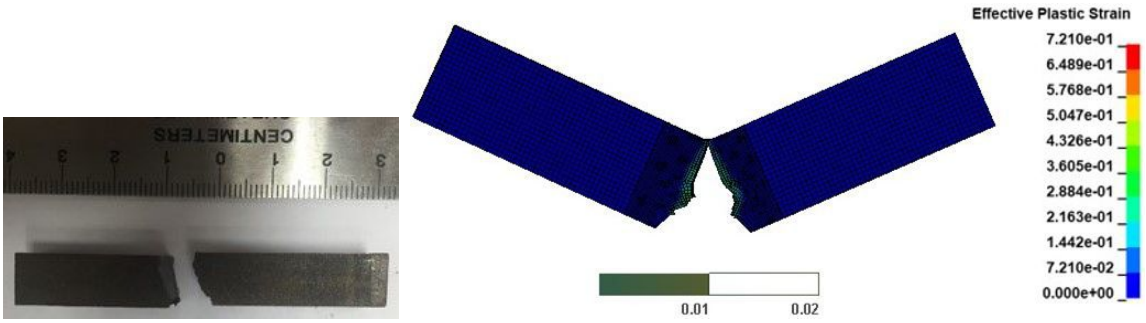

(a) Experimental (b) FEA simulation

Fig. 5.5. Fracture surface and effective plastic strain at 298 K

There has been predominantly ductile failure of the specimen tested at 723 K (shown in Fig. 5.6) as the fracture surface is a significant level of convexity. The effective plastic strain is distributed beyond the refined mesh zone and has a maximum value of 1.136 m/m. Based on the comparison of the convexity and effective plastic strain, this specimen behaved more ductile than the 77 K and 298 K specimens.

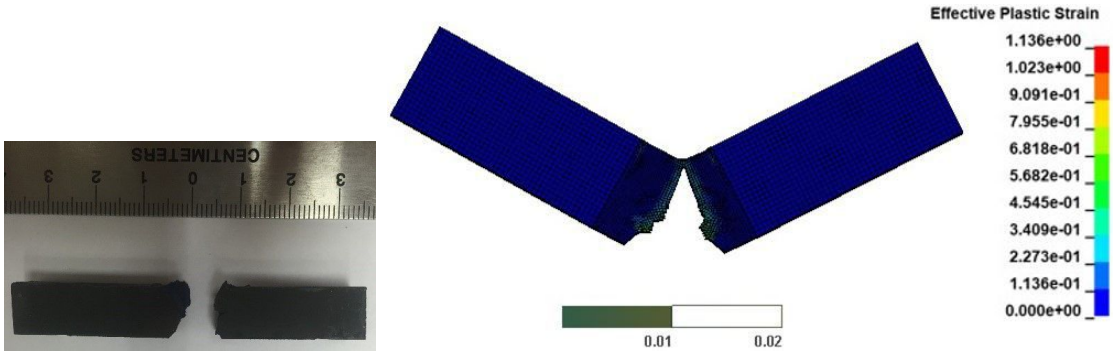

(a) Experimental (b) FEA simulation

Fig. 5.6. Fracture surface and effective plastic strain at 723 K

5.4 Charpy impact energy

5.4.1 Experimental

For the experimental Charpy impact test, the recorded impact energy at 77 K, 298 K and 723 K were 0.00 J/cm^2, 6.78±4.07J/cm^2 and 50.84±3.39J/cm^2 respectively as shown in Table 5.1. There was a suspected anomaly in the 77 K specimen reading as the material is expected to absorb some of the kinetic energy that would lead to an increase in the internal energy, however, it is highly suspicious that the accuracy of the instrument is insufficient to detect this small change. Energy loss in the system may be attributed to internal resistance of the gauge, friction in the bearing of the pendulum, air resistance, sound and slip between the specimen and the anvil.

Table 5.2.
Experimental Charpy impact test results.

Temperature of Specimen, K	**Impact Energy,** J/cm^2
77	0.00
298	6.78±4.07
723	50.84±3.39

5.4.2 Numerical simulation

Upon impact, the internal energy rapidly increases and plateaus to a constant value, as shown in Fig. 5.7. This constant value of internal energy at the peak is termed as the impact energy. The impact energy at 77 K, 298 K and 723 K are 1.05 J/cm^2, 10.46 J/cm^2 and 47.07J/cm^2 respectively.

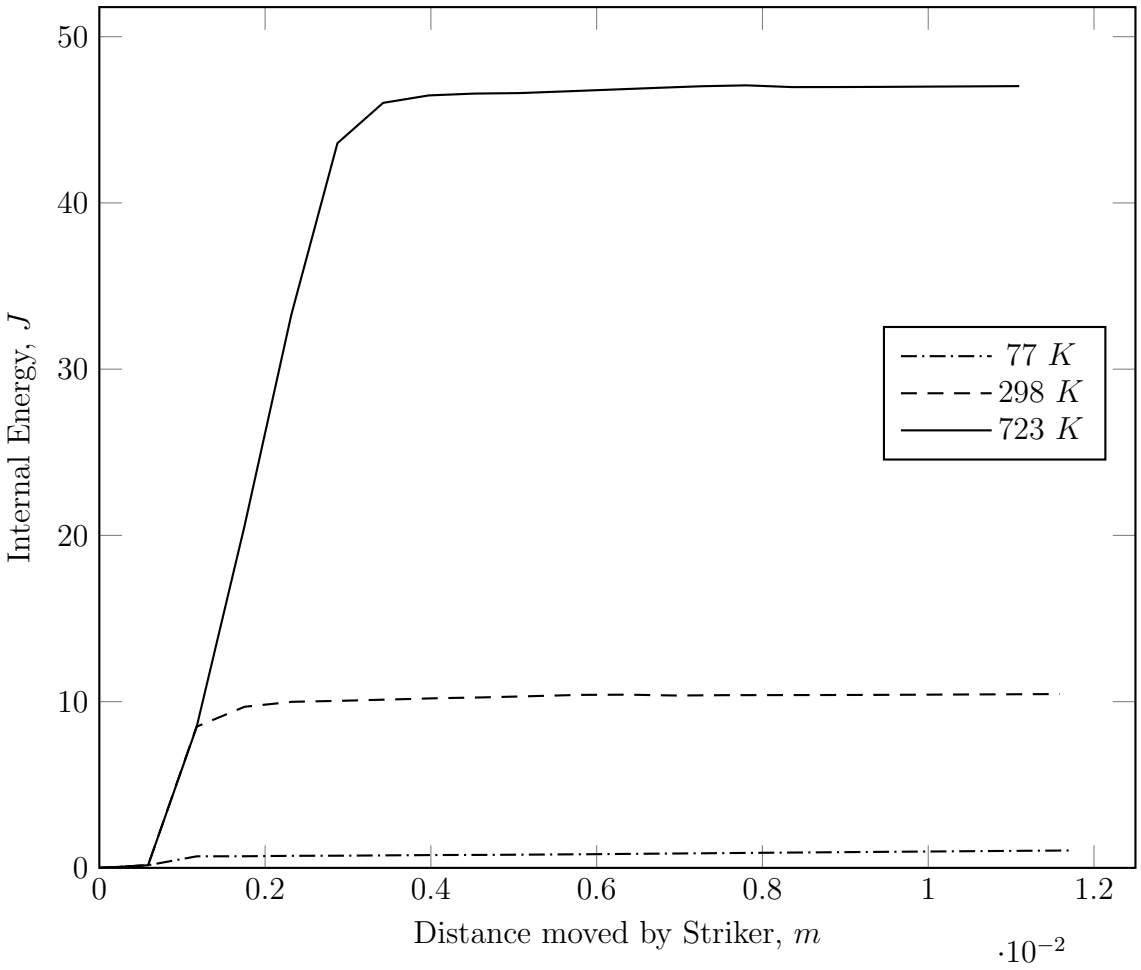

Fig. 5.7. Numerical modeling impact energy at 77 K, 298 K and 723 K

5.4.3 Comparison between experimental and numerical modeling impact energy

The impact energy from the experimental and numerical simulation of the Charpy impact test show good agreement as shown in Fig. 5.8.

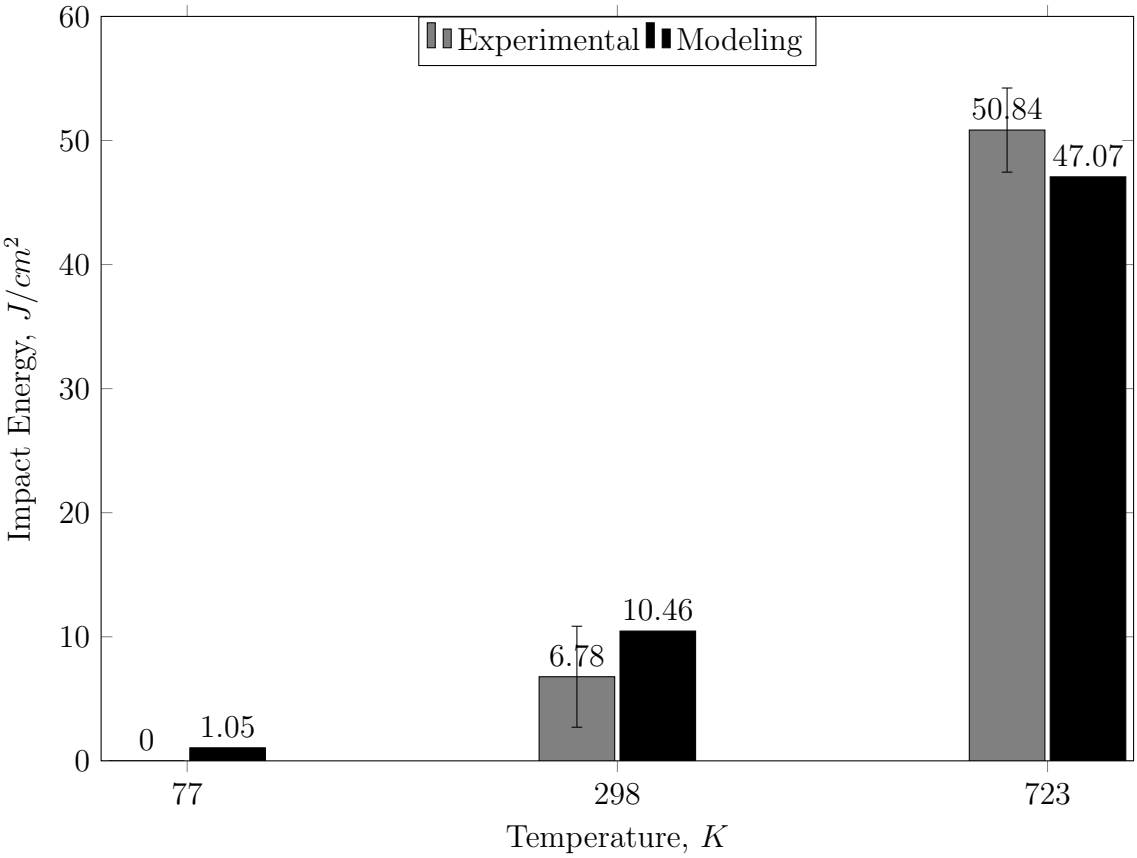

Fig. 5.8. Comparison of impact energy between experimental and numerical modeling.

The numerical modeling impact energy was expected to be more than that of the experimental given that rigid body assignments were specified for the anvil and striker and frictionless surfaces were specified for the specimen-to-anvil and striker-to-specimen interfaces; and in reality, these may not be totally true for the experimental Charpy impact test. However, the experimental impact energy was greater than the simulated values for the room and high temperature scenarios. This may have

arisen out of modeling errors. Given that nonlinear finite element analysis was used, the accuracy was dependent on the load increments, at lower load increment, the analysis time was prohibitively high, however, when these were raised, convergence was slow. Hence, based on trial and error, the time steps were chosen that would satisfy both computation time reduction and faster convergence, resulting in some loss of accuracy in modeling. Other errors include convergence criteria that is inherent in the structural analysis program and accuracy of the material model adopted.

5.4.4 Impact energy comparison between 3D printed and wrought 15-5 stainless steel

There is limited literature on the toughness of 3D printed 15-5 stainless steel as well as the wrought counterpart at the temperatures tested. Hence, in this section, the comparison was made between the impact energy of 3D printed and wrought 15-5 stainless steel at room temperature.

At room temperature, both the experimental and numerical modeled impact energy of 3D printed stainless steel (i.e. 10.85 J/cm^2 and 10.46 J/cm^2 respectively) measured very well against its wrought counterpart 10.0 J/cm^2 [25].

5.5 Ballistic impact simulations

5.5.1 Effective plastic strain

The penetration of the missile through the plate at 77 K may be described as a predominantly shear or brittle failure as shown in Fig. 5.9. The surfaces appeared to have been sheared by the missile and the effective plastic strain is concentrated only around the penetration boundary, hence leaving a punched hole. Part of the plate has also been dislodged as a result of brittle failure upon impact. The effective plastic strain of 0.57 m/m is the lowest amongst the three temperatures.

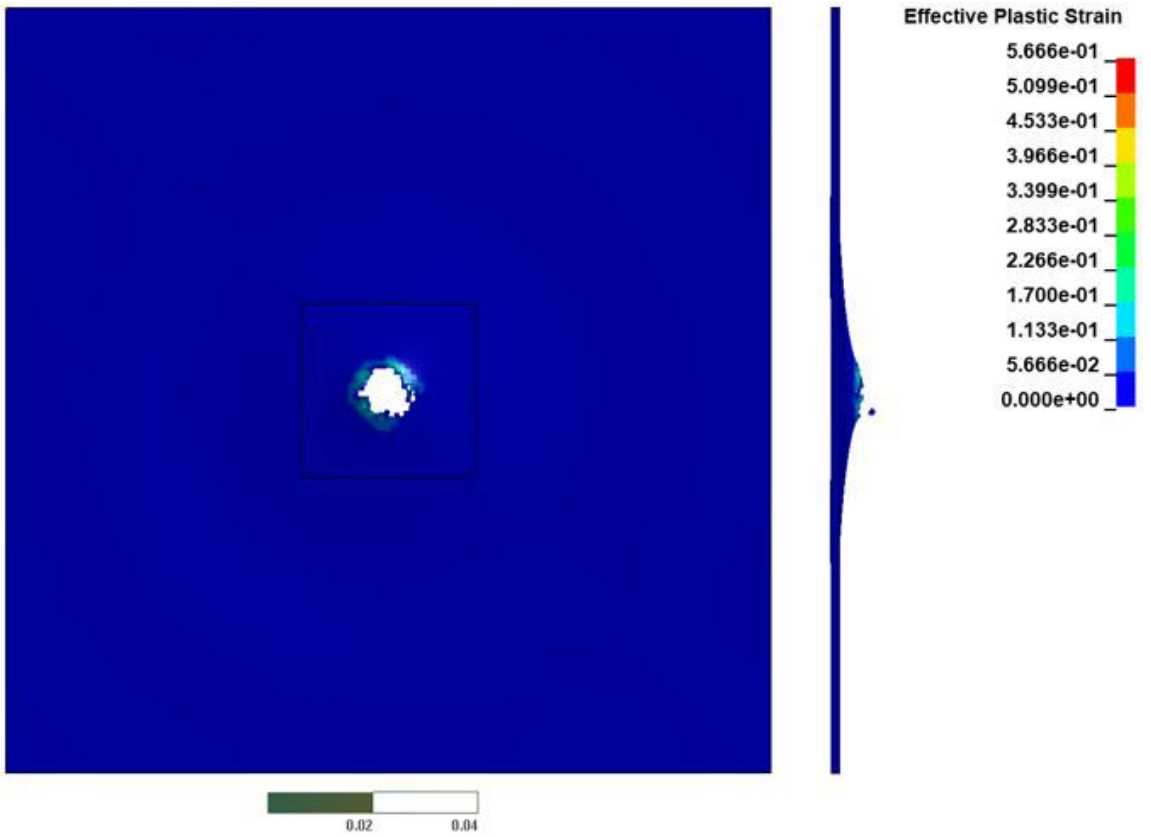

Fig. 5.9. Effective plastic strain of plate at 77 K.

Based on the observation of the fracture surface, the penetration of the missile through the plate at 298 K may be described as a combination of shear or brittle and ductile failure as shown in Fig. 5.10. Unlike the punched hole in the plate as in the 77 K plate, part of the impact zone folded and covered the penetration upon exit of the missile. Also, in comparison to the plate penetration at 77 K, the effective plastic strain zone extended further beyond the point of penetration. The effective plastic strain of 1.57 m/m was more than double the value recorded at 77 K but less than the simulation at 723 K.

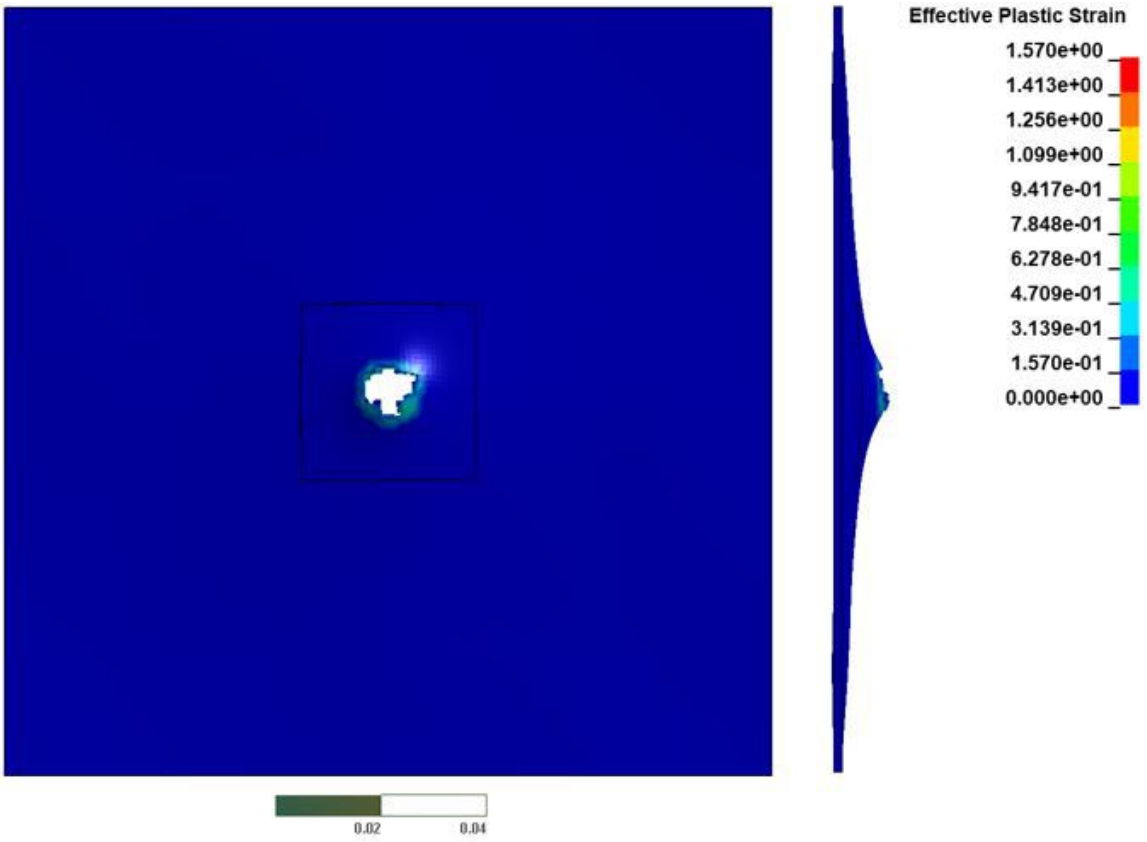

Fig. 5.10. Effective plastic strain of plate at 298 K.

The penetration of the missile through the plate at 723 K may be described as a predominantly ductile failure as shown in Fig. 5.11. The effective plastic strain zone is the furthest of all three simulations. Also, the effective plastic strain of 2.48 m/m approximately five times that recorded at 77 K and one and a half times the value at 298 K. Therefore, based on these observations, the plate was more ductile at 723 K than at 298 K and 77 K.

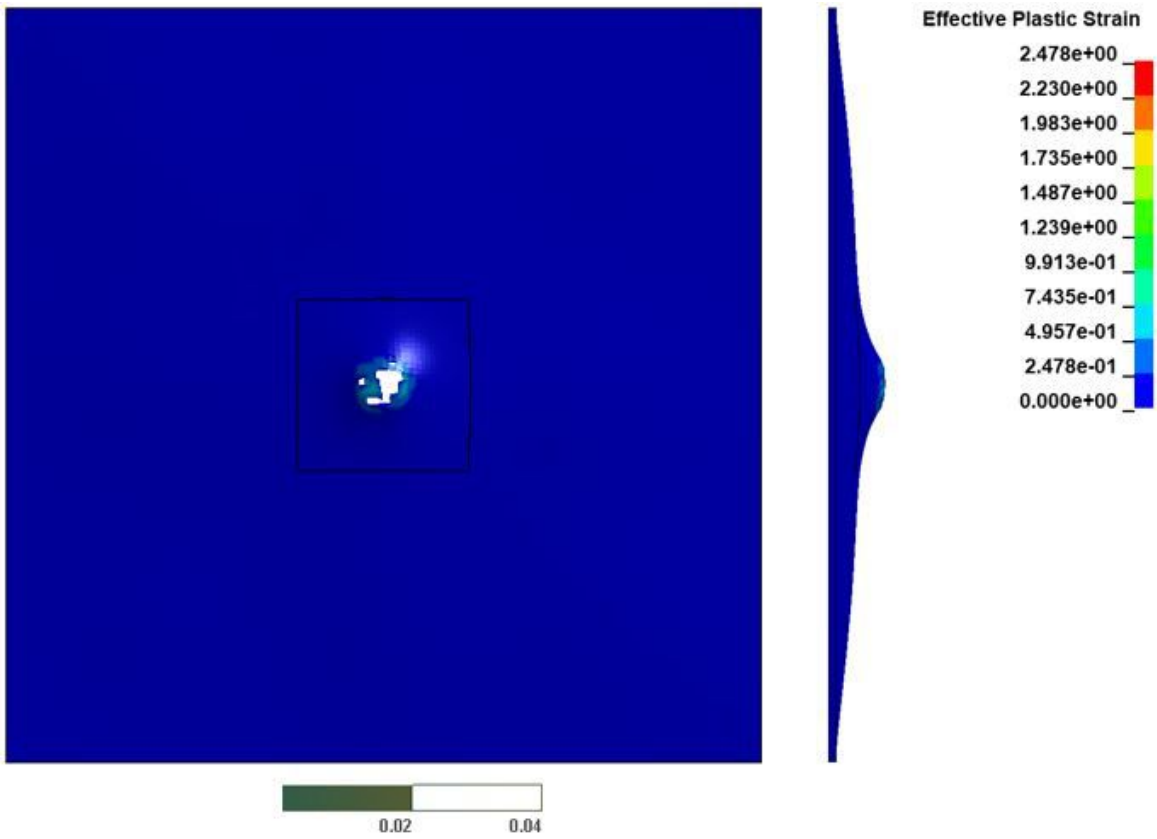

Fig. 5.11. Effective plastic strain of plate at 723 K.

5.5.2 z-displacement of plate

The displacement of the plate in the direction of the missile indicates its ability to stretch upon impact. This deformation is therefore correlates to the energy dissipation of a missile, however, excessive deformation may not be desirable due to serviceability constraints (internal parts and personnel).

The maximum z-displacement of the plate recorded at 77 K was 6.94 mm as shown in Fig. 5.12. The displacement pattern was circular, indicating that there was minimal tension field or membrane action. Tension field or membrane action is the post yield behavior of plates that are subjected to out of plane concentrated loads and is an indicator of the toughness of a material. In the case of the 77 K specimen,

the stiffness at the boundaries had minimal influence on the displacement pattern indicating that tension field action was not predominant, but the direct loading of the missile.

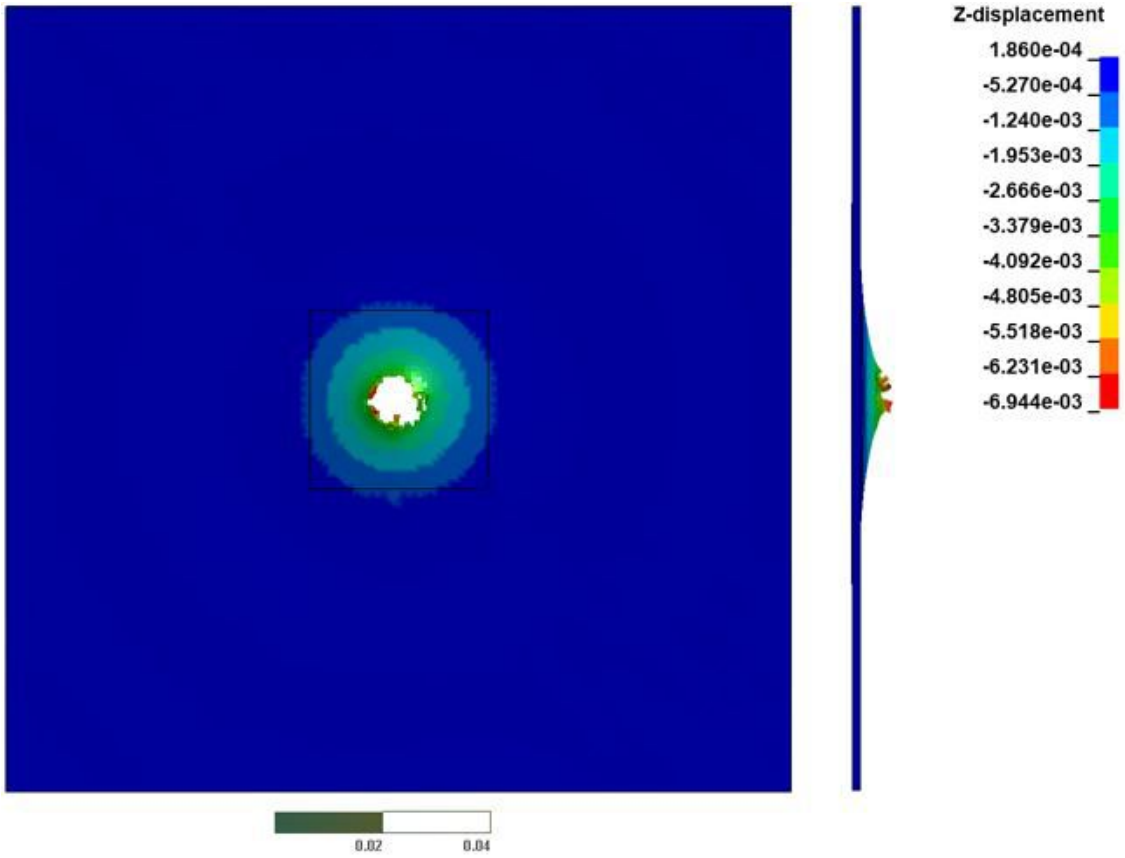

Fig. 5.12. z-displacement of plate at 77 K.

The maximum z-displacement of the plate at 298 K was 10.93 mm which was nearly double that at 77 K as shown in Fig. 5.13. The displacement pattern indicate larger displacement towards the center span of the plate, hence the is greater influence of the tension field or membrane effect than at 77 K. Also, the displacement is minimal towards the higher stiffness of the corners indicating that there is some measure of ductility that sustain the tension field, but not sufficient to create an independent horizontal load carrying system.

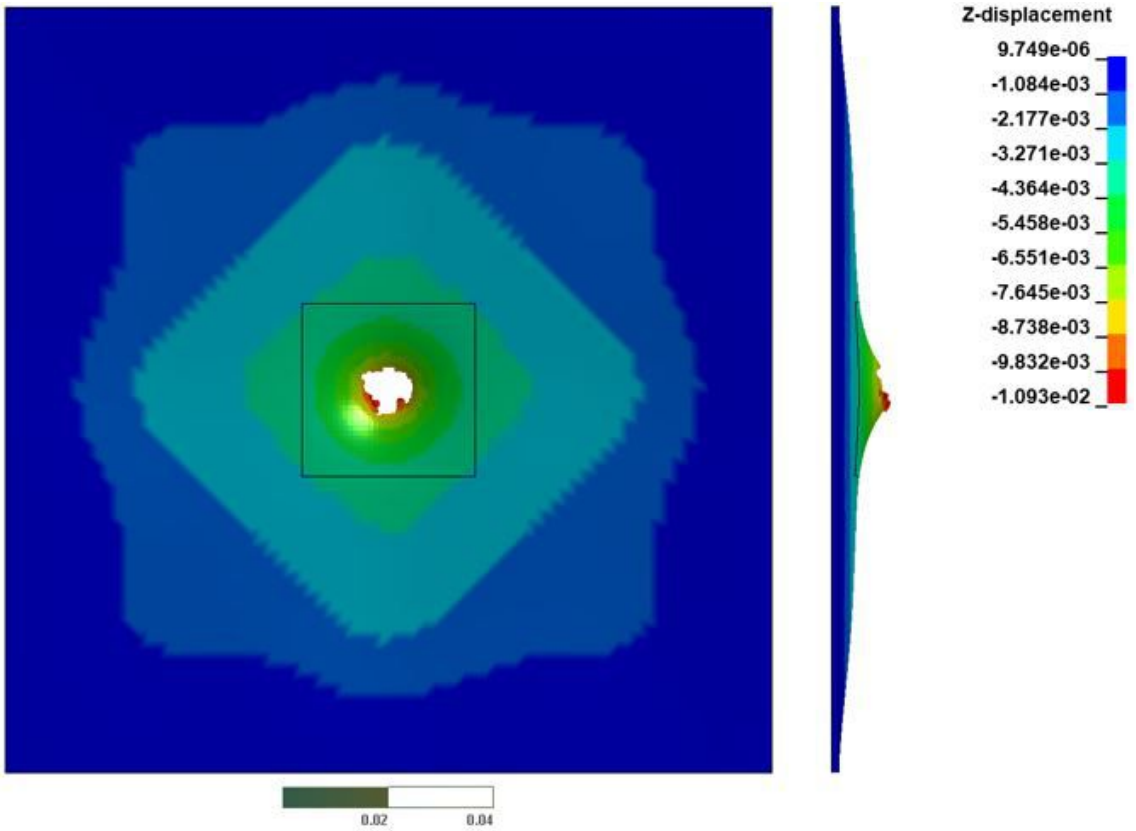

Fig. 5.13. z-displacement of plate at 298 K.

The maximum z-displacement of the plate at 723 K was 10.50 mm as shown in Fig. 5.14. This value appeared less than the total deflection of the plate at 298 K, however, it was observed that generally, there was a larger overall plate deflection, but the point of exit was not torn as the room temperature plate, the latter of which may indicate a superficially higher deflection. The displacement pattern indicates predominance of tension field or membrane action, the in plane effect of this action indicates a large span between the stiff vertices. The maximum spread of displacement is therefore between each vertex. This is due to the increase in ductility in the material that enable the formation of the tension field. Given that tension field or membrane action acts in plane and not in the direction of the missile,and is a post yield strength of the plate, an increase in its effect is correlated to an increase in ductility or toughness of the material.

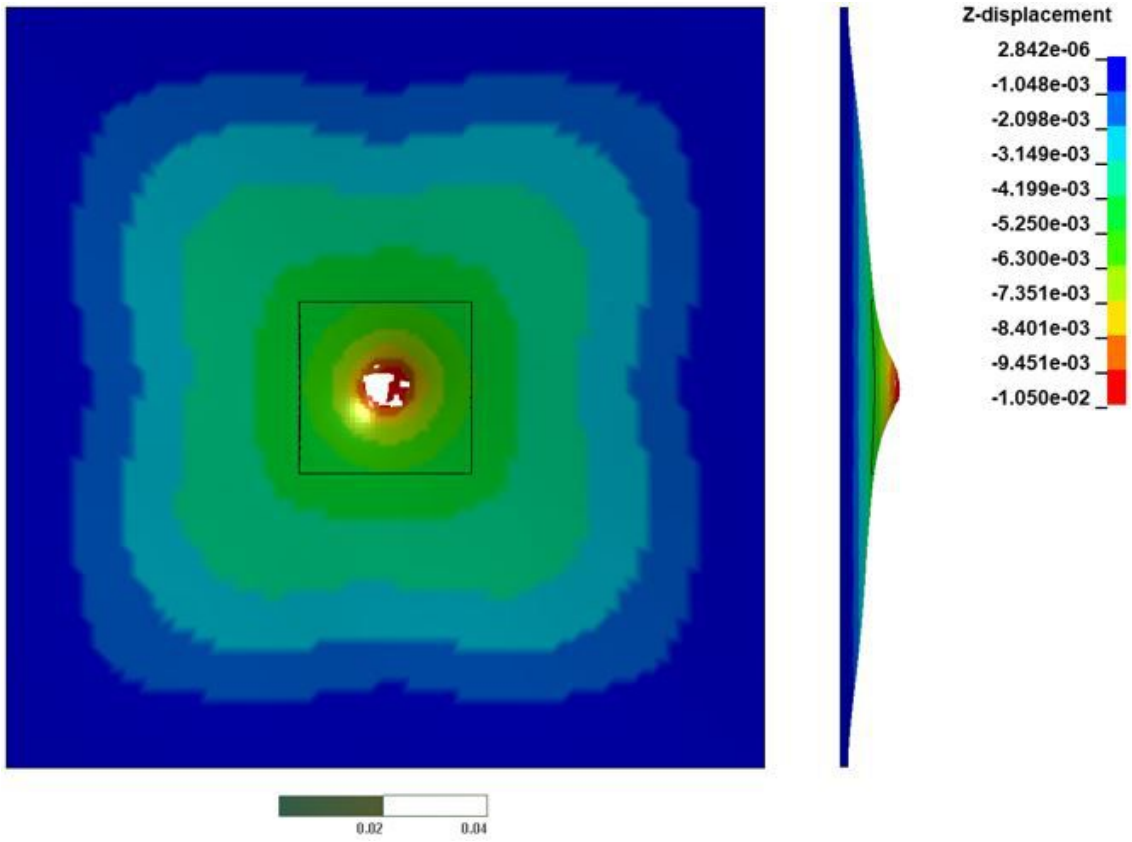

Fig. 5.14. z-displacement of plate at 723 K.

5.5.3 Exit velocity of missile

Materials used in the line of defense is required to retard or stop a high velocity missile upon impact, therefore the exit velocity has been investigated to determine the effectiveness of the 3D printed 15-5 stainless steel. At 77 K the exit velocity was 292 ms^{-1} as shown in Fig. 5.15, which is relatively high compared to the initial velocity of 300 ms^{-1}; hence, the 1.5 mm thick plate was not effective in significantly reducing the velocity of the missile.

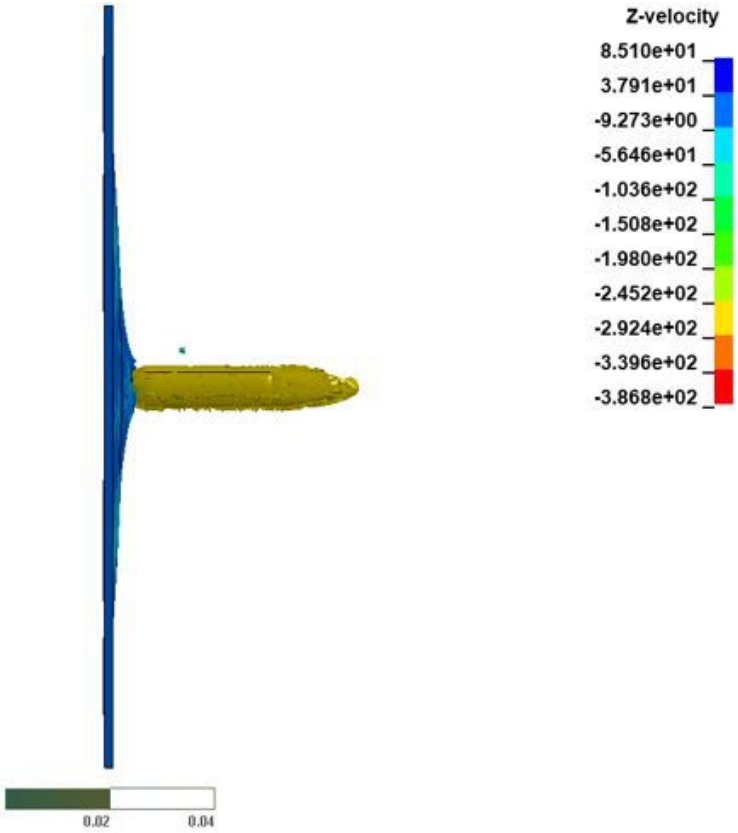

Fig. 5.15. Exit velocity of missile at 77 K.

At 298 K, the exit velocity was 187 ms^{-1} in Fig. 5.16 which represent about 62 % of the initial velocity of the missile. As with the impact simulated at 77 K, the exit velocity is still significantly high and may not be desirable in service.

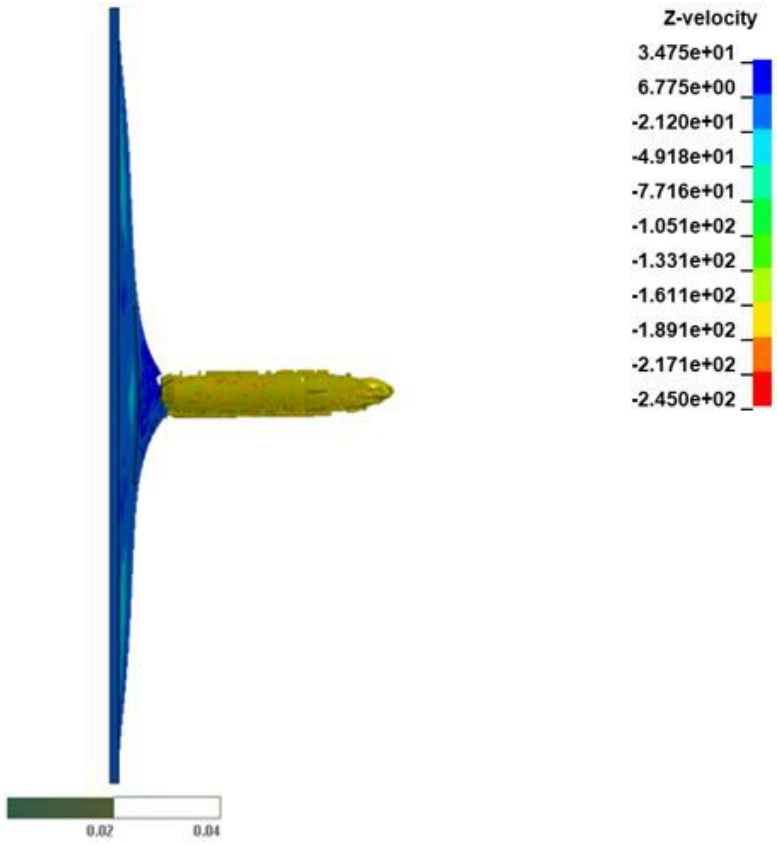

Fig. 5.16. Exit velocity of missile at 298 K.

The exit velocity at 723 K was 102 ms^{-1} as shown in Fig. 5.17 which is 34% of the initial velocity of the missile. Hence it at high temperature, the 3D printed plate has significantly reduced the velocity of the missile. However, the missile was not embedded or necessarily stopped by the plate.

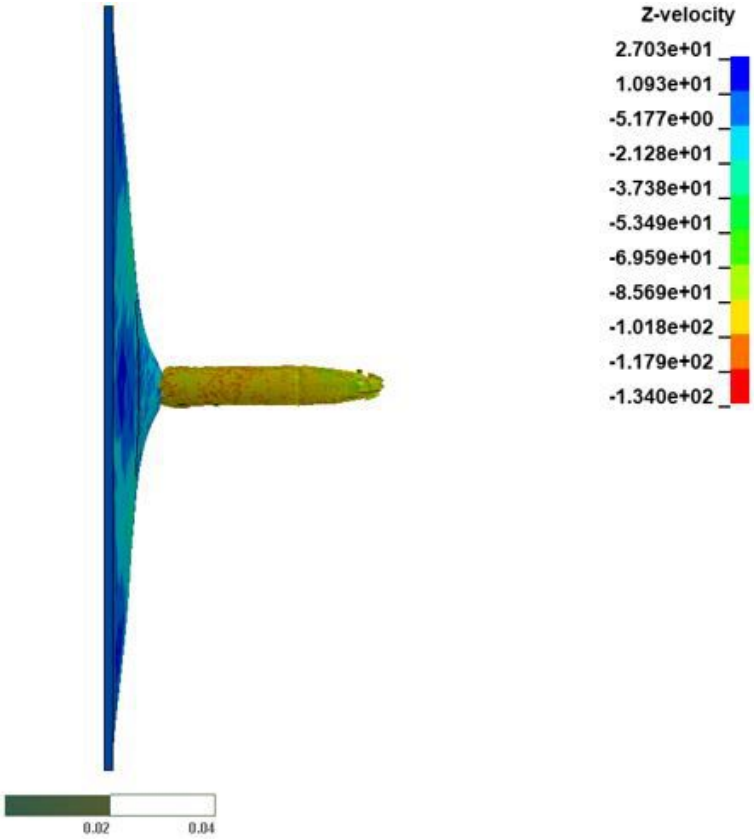

Fig. 5.17. Exit velocity of missile at 723 K.

It can be observed that generally as the temperature of the plate is increased, the exit velocity of the missile decreases indicating that greater effectiveness of the plate in dissipating the kinetic energy of the missile at higher temperatures.

5.5.4 Impact energy comparison

Similar to the Charpy impact test, the impact energy of the plate is analogous to the that of the specimen. In a ballistic impact simulation, the impact energy gives an indication of how much kinetic energy of the missile is converted to internal energy of the plate.

The impact energy recorded at 77 K was 40 J was shown in Fig. 5.18. When averaging the impact energy, the peak value of internal energy was used as the plate

was observed oscillating back and forth as the missile exited. At 298 K, the impact energy of 134 J was more than three times the impact energy recorded at 77 K. Furthermore, the impact energy at 723 K was 152 J. Hence, similar to the Charpy impact test, the plate impact energy has been observed to increase at increasing temperature.

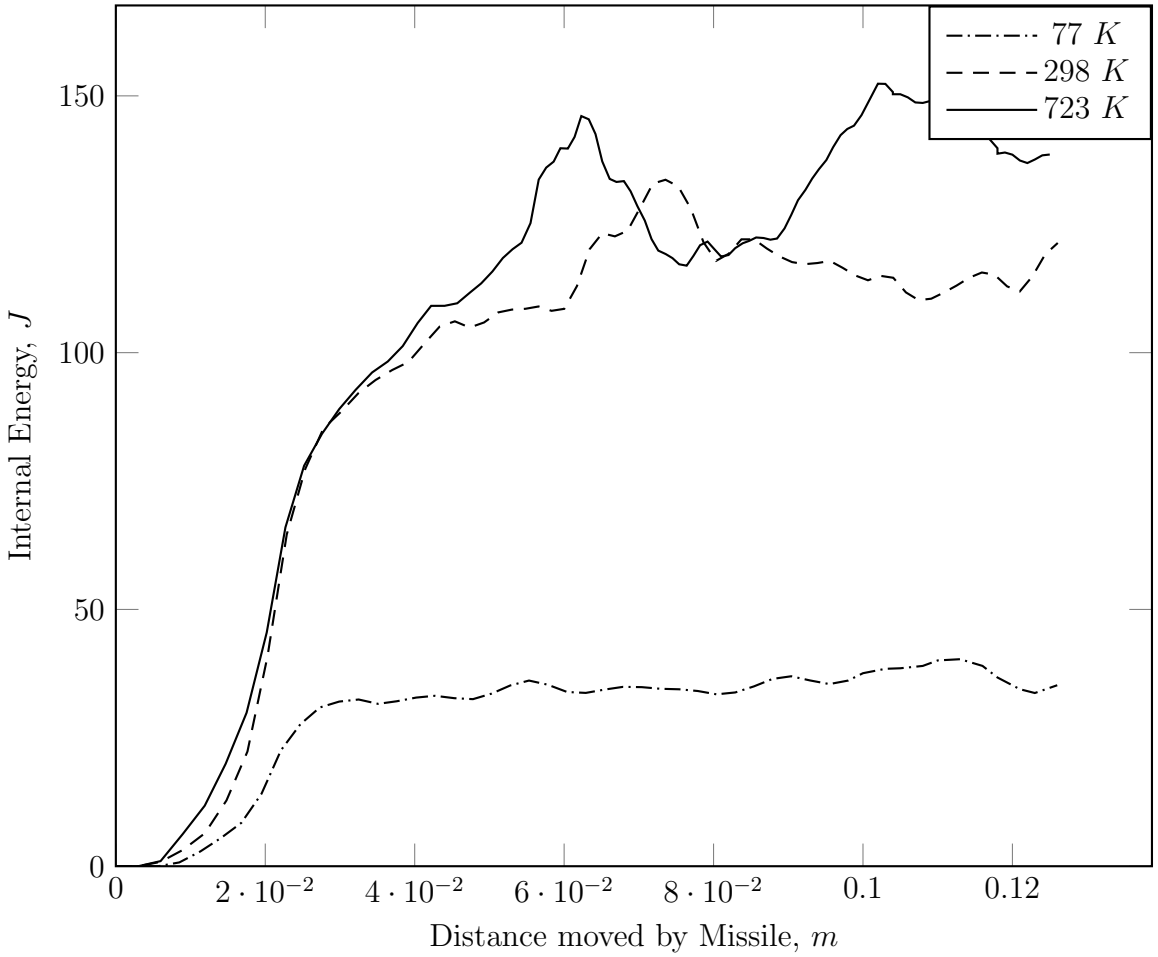

Fig. 5.18. Ballistic simulation impact energy at 77 K, 298 K and 723 K.

For both low and room temperatures, the oscillation of the plate indicating there is kinetic energy in the plate, hence the highest value was adopted assuming that the maximum internal energy that could be reached by the plate is the impact energy.

6. SUMMARY

A combined experimental and numerical modeling approach has adopted to investigate the temperature-dependent impact properties of 3D printed 15-5 stainless steel. The results are summarized as follows:

(1) The microsurface analysis (OM and SEM), visual inspection of the fracture surface and corresponding impact energy from the Charpy impact test indicate a transition from brittle to ductile failure of the specimens as the temperature was increased. Hence, the toughness of 3D printed 15-5 stainless steel increased with an increase in temperature.

(2) Experimental and numerical modeling impact energy for the Charpy impact test show good agreement. At 77 K, the impact energy was 0.00 J/cm^2 whereas numerical modeling value was 1.05 J/cm^2. For the room temperature (298 K), the experimental recorded impact energy was 6.78$\pm$4.07 J/cm^2 whereas the numerical modeling result was 10.46 J/cm^2. Also, at high temperature (723 K), the experimental impact energy was 50.84$\pm$3.39 J/cm^2 whereas the simulated impact energy was 47.07 J/cm^2.

(3) The experimental and numerical Charpy impact energy of 3D printed 15-5 stainless steel at room temperature show good agreement with the conventionally manufactured counterpart.

(4) For the ballistic impact simulation for 3D printed 15-5 stainless steel at low temperature (77 K), the missile penetrated the plate in a predominantly shear failure upon visual inspection of the path through the sheet. The corresponding impact energy of the plate was 40 J which is relatively small compared to the kinetic energy of the missile upon impact i.e. 1011 J. An effective plastic strain was 0.56 m/m and the maximum deflection was 6.9 mm. The exit velocity was 292 ms^{-1} which is

close to the initial velocity of 300 ms^{-1}, hence a high percentage of the initial kinetic energy of the missile was preserved after impact with the plate.

(5) For the ballistic impact simulation for 3D printed 15-5 stainless steel at room temperature (298 K), a higher impact energy than at (77 K) was recorded i.e. 134 J (more than 3 times that at 77 K). The effective plastic strain and deflection were almost double the values at 77 K. i.e. 1.57 m/m and 10.93 mm respectively. The exit velocity of the missile at 298 K was 187 ms^{-1} which is still relatively high i.e. approximately 62% of the initial velocity.

(6) For the ballistic impact simulation for 3D printed 15-5 stainless steel at high temperature (723 K), the highest impact energy amongst the three simulations was recorded i.e. 152 J. An effective plastic strain of 2.48 m/m was 41% than that recorded at 298 K, whereas the maximum deflection of 10.50 mm was fractionally lower due to difference in behavior of penetrated section edges. The exit velocity was 102 ms^{-1} which is substantially lower than the initial velocity but may still be too high for consideration in defense.

(7) Consistent with the Charpy impact test, the ballistic impact simulation indicate that there is an increase in toughness of the 3D printed 15-5 stainless steel plate with an increase in temperature. The 3D printed 15-5 stainless steel plates in its current configuration may not be effective in significantly reducing the initial velocity of a missile at the specified temperatures, although generally the exit velocity decreased with an increase in temperature.

7. RECOMMENDATIONS

The recommendations for improvement of this study are as follows:

(1) The use of an experimental Charpy impact tester with higher accuracy may be useful in testing at cryogenic temperatures given the small impact energy anticipated.

(2) In order to determine the holistic behavior of 3D printed 15-5 stainless steel, it is it may be useful to investigate the impact properties in all possible printing orientations and compare the impact values to conventionally manufactured equivalent for real-world application where the material may be assumed to be isotropic.

(3) To improve the accuracy and representation of the J-C parameters for 3D printed 15-5 stainless steel, published literature recommend quasi-static tensile test, Taylor cone test and dynamic Hopkinson bar test. The design of experiments, curve fitting and standard optimization techniques may be useful in extracting J-C data from the tests.

(4) Prepare and print more samples and set up a design of experiment to validate results and to corroborate the numerical modeling that may then be codified.

(5) It may be useful to explore changing the plate thickness and modifying the support conditions in order to prevent the missile from penetrating the plate as in this study, there was full penetration and the minimum exit velocity recorded was 102 ms^{-1} which is significantly high.

REFERENCES

REFERENCES

[1] ASTM, "Standard test methods for notched bar impact testing of metallic materials," ASTM International, West Conshohocken, PA, ASTM E23-16b, 2016.

[2] H. Kodama, "A scheme for three-dimensional display by automatic fabrication of three-dimensional model," *J. IEICE*, vol. 64, pp. 1981–4, 1981.

[3] H. Kodama, "Automatic method for fabricating a three-dimensional plastic model with photo-hardening polymer," *Review of scientific instruments*, vol. 52, no. 11, pp. 1770–1773, 1981.

[4] E. Matias and B. Rao, "3d printing: On its historical evolution and the implications for business," in *Management of Engineering and Technology (PICMET), 2015 Portland International Conference on*. IEEE, 2015, pp. 551–558.

[5] L. Toth, H.-P. Rossmanith, and T. A. Siewert, "Historical background and development of the charpy test," in *European Structural Integrity Society*. Elsevier, 2002, vol. 30, pp. 3–19.

[6] O. Yasuhisa, T. Yu, M. Mano, and T. Okada, "Design of ship hull structures: A practical guide for engineers," *Verlag Berlin Heidelberg: Springer*, pp. 319–333, 2009.

[7] Z. Pitrmuc, J. imota, J. Uban, and L. Bernek, "Influence of process parameters and part orientation on mechanical properties for dmls manufactured stainless steel aisi 316l," *Conferences of Student Creative Activity, 2017*, p. 09, 2017.

[8] J. W. Hendrickson, "Use of direct metal laser sintering for tooling in high volume production," 2015.

[9] M. Montero Sistiaga, S. Nardone, C. Hautfenne, and J. Van Humbeeck, "Effect of heat treatment of 316l stainless steel produced by selective laser melting (slm)," in *Proceedings of the 27th Annual International Solid Freeform Fabrication Symposium-An Additive Manufacturing Conference*, 2016, pp. 558–565.

[10] "Asm aerospace specification metals inc." (Date last accessed 06-March-2018). [Online]. Available: http://asm.matweb.com/search/SpecificMaterial.asp?bassnum=MQM15AI

[11] "Eos stainlesssteel ph1 for eosint m 270," (Date last accessed 06-March-2018). [Online]. Available: http://gpiprototype.com/images/PDF/EOS-StainlessSteel-PH1.pdf

[12] S. Sagar, Y. Zhang, L. Wu, H.-Y. Park, J.-H. Lee, Y.-G. Jung, and J. Zhang, "Room-temperature charpy impact property of 3d-printed 15-5 stainless steel," *Journal of Materials Engineering and Performance*, pp. 1–5, 2018.

[13] "Creo parametric 2.0, 2012," (Date last accessed 06-March-2018). [Online]. Available: http://www.lstc.com/download/manuals

[14] "Eosint m 270," (Date last accessed 06-March-2018). [Online]. Available: https://dmlstechnology.com/images/pdf/EOSINT M 270.pdf

[15] "Eosint m materials for direct metal laser-sintering (dmls)," (Date last accessed 11-April-2018). [Online]. Available: http://www.3dimpuls.com/sites/default/files/dok-book/m-materials-en.pdf

[16] "Instron.us, 2018," (Date last accessed 06-March-2018). [Online]. Available: http://www.instron.us/-/media/literature-library/products/2005/05/impact-pendulum-test-systems.pdf?la=en-US

[17] "Livermore software technology corporation, ls-pre/post v1.o beta," (Date last accessed 06-March-2018). [Online]. Available: http://www.dynasupport.com/manuals/additional/ls-pre-post-v1.0-manual

[18] G. R. Johnson, "A constitutive model and data for metals subjected to large strains, high strain rates and high temperatures," in *Proceedings of the 7th International Symposium on Ballistics, The Hague, Netherlands, 1983*, 1983.

[19] W. T. Graves, D. Liu, and A. N. Palazotto, "Topology optimization of a penetrating warhead," in *57th AIAA/ASCE/AHS/ASC Structures, Structural Dynamics, and Materials Conference*, 2016, p. 1509.

[20] G. R. Johnson and W. H. Cook, "Fracture characteristics of three metals subjected to various strains, strain rates, temperatures and pressures," *Engineering fracture mechanics*, vol. 21, no. 1, pp. 31–48, 1985.

[21] A. J. Gross *et al.*, "Towards the predictive modeling of ductile failure," Ph.D. dissertation, 2015.

[22] "Livermore software technology corporation, ls-dyna r10.0 volume i," (Date last accessed 06-March-2018). [Online]. Available: http://www.lstc.com/download/manuals

[23] "Dassault systèmes 3d cad design software, solidworks," (Date last accessed 06-March-2018). [Online]. Available: http://www.solidworks.com

[24] T. Warlow, *Firearms, the law, and forensic ballistics*. CRC Press, 2016.

[25] "Azo materials," (Date last accessed 19-March-2018). [Online]. Available: https://www.azom.com/article.aspx?ArticleID=6786\#4

VITA

VITA

List of publications

S. Sagar and J. Zhang, "Charpy Impact Test of 3D Printed Stainless Steel A Combined Experimental and Modeling Study," proceedings from POWDERMET2017 Conference - Advances in Powder Metallurgy and Particulate Materials, pp. 962-970, 2017. Metal Powder Industries Federation, Princeton, NJ 08540-6692, USA.

S. Sagar, Y. Zhang, L. Wu, H.-Y. Park, J.-H. Lee, Y.-G. Jung, and J. Zhang, "Room-temperature Charpy impact property of 3D printed 15-5 stainless steel," Journal of Materials Engineering and Performance, pp. 15, 2018.

Y. Zhang, S. Sagar, L. Wu, H.-Y. Park, Y.-G. Jung, and J. Zhang, "Temperature-Dependent Charpy impact property of 3D printed 15-5 stainless steel," Journal of Materials Engineering and Performance, (submitted).

List of presentations

IUPUI Research Day, March 2017, Hine Hall, IUPUI: Poster Presentation: S. Sagar, and J. Zhang, "Charpy Impact Test of 3D-Printed 15-5 Stainless Steel".

POWDERMET 2017, June 2017, Las Vegas (National Science Foundation (NSF) grant): Poster Presentation: S. Sagar and J. Zhang, "Charpy Impact Test of 3D Printed Stainless Steel - A Combined Experimental and Modeling Study".

Midwest Student in Engineering Mechanics, March 2018, Purdue University, West Lafeyette: Powerpoint Presentation: S. Sagar and J. Zhang, "Temperature-Dependent Impact Properties of 3D Printed 15-5 Stainless Steel".

IUPUI Research Day, April 2018, Hine Hall, IUPUI: Poster Presentation: S. Sagar, and J. Zhang, "Temperature-Dependent Charpy Impact Properties of 3D Printed 15-5 Stainless Steel".